9

Review article

Chun Li, Zhen Liu, Jie Chen, Yan Gao, Meili Li and Qing Zhang*

Semiconductor nanowire plasmonic lasers

https://doi.org/10.1515/nanoph-2019-0206 Received July 2, 2019; revised October 7, 2019; accepted October 7, 2019

Abstract: Semiconductor nanowires (NW) hold great promise for micro/nanolasers owing to their naturally formed resonant microcavity, tightly confined electromagnetic field, and outstanding capability of integration with planar waveguide for on-chip optoelectronic applications. However, constrained by the optical diffraction limit, the dimension of semiconductor lasers cannot be smaller than half the optical wavelength in free space, typically several hundreds of nanometers. Semiconductor NW plasmonic lasers provide a solution to break this limitation and realize deep sub-wavelength light sources. In this review, we summarize the advances of semiconductor NW plasmonic lasers since their first demonstration in 2009. First of all, we briefly look into the fabrication and physical/chemical properties of semiconductor NWs. Next, we discuss the fundamentals of surface plasmons as well as the recent progress in semiconductor NW plasmonic lasers from the aspects of multicolor realization, threshold reduction, ultrafast modulation, and electrically driven operations, along with their applications in sensing and integrated optics. Finally, we provide insights into bright perspectives and remaining challenges.

Keywords: semiconductor nanowire; plasmonic laser; nanoplasmonics; sub-wavelength optics; photon-plasmon interaction.

Zhen Liu, Yan Gao and Meili Li: Department of Materials Science and Engineering, College of Engineering, Peking University, Beijing 100871, PR China

1 Introduction

Rapid development of semiconductor lasers has significantly expanded frontier research on semiconductor photonics from fundamental sciences to industrial technologies, in which device miniaturization has been a long-standing and continuous pursuit. From the creation of edge-emitting lasers [1], vertical-cavity surface-emitting lasers [2-4], microdisk lasers [5-7], and photonic crystal lasers [8–10] to the discovery of nanowire (NW) lasers [11–13], the volume of semiconductor lasers has gradually reduced, which is still constrained by the diffraction limit and cannot be lower than half the optical wavelength (λ) , typically several hundred nanometers. This size is an order of magnitude larger than the feature size of modern transistors, which would cause integration mismatch and serious energy dissipation, and thus limit practical applications of micro/nanolasers [14]. In the past decade, a new type of small lasers, based on surface plasmons (SPs), the so-called plasmonic laser, has received widespread attention for achieving deep sub-wavelength laser sources and advancing the development of nano-optics [15-18]. In plasmonic lasers, optical waves can couple with SPs occurring at the metal-dielectric interface and store their energies in free electron oscillations. As a result, the physical dimension of the plasmonic cavity can be compressed to the nanometer scale, ultimately enabling the simultaneous amplification of photons and SPs in analogy with the photonic lasing from pure dielectric materials [19–21]. Meanwhile, strong photon-plasmon interactions significantly enhance the local field, which allows the plasmonic laser to deliver high power density, low theoretical consumption, and fast response, which are promising for regulating linear and nonlinear optical processes [22–27]. So far, the minimum size of the plasmonic laser is comparable to that of the metal-oxide-semiconductor field effect transistor (~10 nm), and the coupling efficiency with silicon waveguide reaches up to 90%, both making the plasmonic laser a great candidate to replace electronic circuits in the semiconductor industry.

So far the plasmonic lasing has been demonstrated in various architectures, which can be mainly divided into four: (1) metallic nanoparticle lasers with threedimensional confinement, such as metal core-dye shell

^{*}Corresponding author: Qing Zhang, Department of Materials Science and Engineering, College of Engineering, Peking University, Beijing 100871, PR China; and The State Key Laboratory of Bioelectronics, Southeast University, Nanjing 210096, PR China, e-mail: Q_zhang@pku.edu.cn. https://orcid.org/0000-0002-6869-0381

Chun Li and Jie Chen: Department of Materials Science and Engineering, College of Engineering, Peking University, Beijing 100871, PR China; and CAS Key Laboratory of Standardization and Measurement for Nanotechnology, CAS Center for Excellence in Nanoscience, National Center for Nanoscience and Technology, Beijing 100190, PR China

laser [28-30]; (2) metal-insulator-semiconductor waveguide (MISW) lasers with two dimensional confinement, e.g. plasmonic NW laser [31]; (3) metal-clad lasers with one-dimensional confinement, e.g. metal-insulator-metal (MIM) laser [32], and (4) plasmonic lattice lasers [33–36]. The semiconductor NW plasmonic laser based on MISW configuration is widely studied owing to its simple structure, facile fabrication, great mode confinement, and long propagation length. Furthermore, semiconductor NWs can also function as interconnection waveguides, photodetectors, and phototransistors, which are building blocks for optical circuits [37, 38]. The compressed size, improved emission performance, and great device integration with on-chip networks enable semiconductor NW plasmonic lasers promising for nanophotonic and nanoelectronic applications.

Here we summarize the physical and chemical properties of semiconductor NWs from the aspects of fabrication, material photophysics, optical gain/loss, and lasing properties in Section 2. Next, we introduce the fundamentals of SP and semiconductor NW plasmonic lasers in Sections 3 and 4. From Section 5–9, the progress of these plasmonic NW lasers is discussed in terms of multicolor operation, threshold reduction, ultrafast response, electrically pumped devices, and down-to-earth applications, respectively. Finally, we highlight future perspectives and challenges that remain in this field.

2 Semiconductor nanowires

Semiconductor NWs, including several quasi-onedimensional nanostructures such as wire, rod, tube, and strip, have received widespread attention since the 1990s [39]. The fabrication of semiconductor NWs is mainly accomplished by breaking the symmetry and guiding anisotropic growth via top-down and bottom-up approaches [40]. Top-down approaches reduce the dimension of bulk materials for micrometer and nanometer structures by chemical or mechanical thinning routes through mechanical deformation, template-based chemical etching, focused ion beam direct writing, and so on [41-43]. Since the size and morphology of NWs can be well controlled in these approaches, they have been widely used for the mass fabrication of Si, Ge, GaAs, InP, and GaN NWs, opening up reproducible pathways for future industrial applications [42, 44–47]. For example, by metal-assisted chemical etching, Zhang et al. reported the fabrication of uniform Si NWs of 50-200 nm in diameter and several tens of micrometers in length from Si wafer precursors, and

without varying the initial doping type and concentration [48]. Bottom-up approaches, including chemical vapor deposition (CVD), physical vapor deposition, hydro- and solvothermal methods, and solution-phase self-assembly, assemble atomic and molecular units into larger complex structures [49–54]. Prior to top-down methods, bottom-up strategies could achieve high-quality products and heterostructure engineering with low density of destructive defects, so they have been employed to grow single-crystal NWs of IV, III-V, and II-VI semiconductors including Si, Ge, GaAs, InP, ZnO, GaN, CdS, CdSe, etc. [49, 51, 55-58]. For example, CsPbBr, NWs synthesized on mica substrates by the CVD method exhibit highly ordered orientation, single-crystal structure, and high emission polarization ratio of up to 0.78 [59]. Using metal organic chemical vapor deposition (MOCVD), Qian et al. fabricated high-quality InGaN/GaN quantum well NWs showing tunable composition and low-threshold, room-temperature, multicolor lasing [60]. Moreover, planar and radial p-n junctions in NW structures have been allowed in bottom-up routes, despite the fact that a homogeneous dopant distribution is still desired in thinner NWs considering the high-level surface states [61, 62]. As solutions, single-ion implantation and epitaxial passivation have improved the doping issue and device stability [63, 64].

Benefited from their extremely high aspect ratio and one dimensionality, NWs are not only of fundamental interest in size and surface effects but also hold great potential for photonic and optoelectronic devices [65-68]. Due to their large refractive index (n) compared to air, NWs can naturally form active Fabry-Pérot (F-P) optical resonators and function as micro/nanolasers via using the semiconductor as the gain medium [69–71]. As illustrated in Figure 1A, photoluminescence is generated as a semiconductor NW is pumped by photons above the bandgap, propagates along the long axis, and is reflected by the two end-facets, and the NW is transformed as an F-P laser if the pump energy is above the threshold. The gain in the NW lasers, g, can be described as $g = \Gamma g_m$, where Γ and g_m are the confinement factor and material gain, respectively. Γ describes the overlap of the optical mode and gain medium, and the photons can be tightly confined in the NWs, leading to a higher theoretical Γ compared with other bulk lasers. g_m is an inherent property of optical gain media and describes their amplification coefficient per unit length; it is ~10²–10⁴ cm⁻¹ for the conventional semiconductors. Optical losses in NW lasers for a round-trip, α , mainly come from the internal loss α_i during light propagation and the mirror loss $\alpha_{\rm m}$ at the end-facets. $\alpha_{\rm i}$ includes loss channels from material absorption, refraction, scattering, and so on. Derived from the light transmission

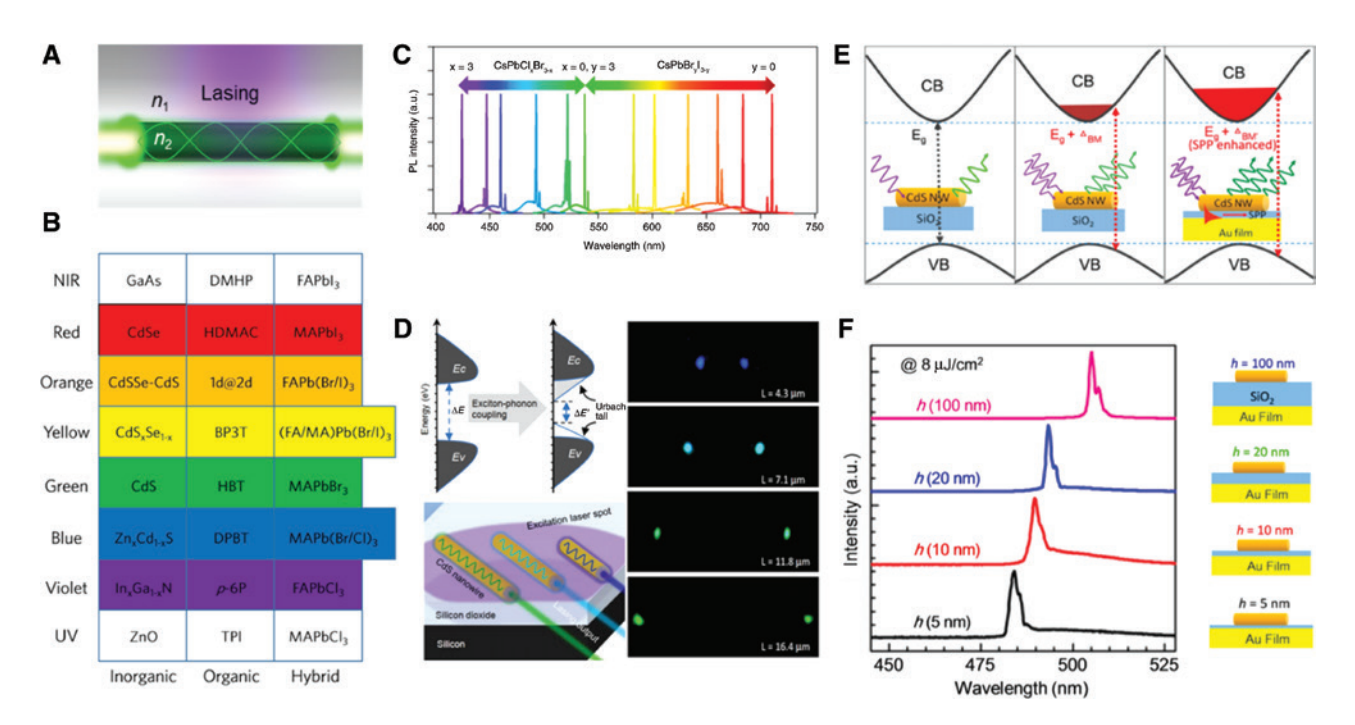


Figure 1: Semiconductor nanowire lasers.

(A) Schematic of semiconductor NW laser. (B) Colorful lasing from UV to NIR in inorganic, organic, and hybrid semiconductor NWs. (C) Broad wavelength-tunable lasing from single-crystal perovskite NWs covering the visible region. Reproduced with permission [72]. Copyright 2016, American Chemical Society. (D) Left: schematic of the Urbach tails at the band edges caused by electron-phonon coupling and various output lasing colors in CdS NW/SiO₂/Si device. Right: optical images of four individual CdS NW lasers with different lengths and colors owing to self-absorption. Reproduced with permission [73]. Copyright 2013, American Chemical Society. (E) Schematic of the three effects on the bandgap energy of undoped semiconductor NWs: without the BM effect, with the BM effect, and the SPP-enhanced BM effect. (F) The lasing peaks of four devices and their illustrations under the same pump fluence. Reproduced with permission [74]. Copyright 2013, American Chemical Society.

at the end-facets, $\alpha_{\rm m}$ can be described as $\alpha_{\rm m} = \frac{1}{L_{\rm o}} \ln \frac{1}{R}$, where *R* is the light reflectivity at the facets, and L_a^{s} is the length of the gain medium, which is equivalent to the NW length. Therefore, the threshold condition of a NW laser is expressed as $\Gamma g_m \ge \alpha_i + \frac{1}{L} \ln \frac{1}{R}$, and as the optical losses are overcompensated by the optical gain provided from stimulated emission, lasing can be established.

The first semiconductor NW lasing was achieved from ZnO NWs on a sapphire (110) substrate fabricated by Au-catalyzed vapor-phase transport process in 2001 [75]. Since then, NW lasers have been widely reported in many semiconductors. Emission color is one of the most important characteristics for lasing, which is briefly located near the electronic bandgap for non-heavily-doped semiconductors. Therefore, selecting gain media with different bandgaps can rationally control the lasing color. As shown in Figure 1B, till now, inorganic semiconductors (i.e. ZnO [49, 75, 76], In_xGa_{1-x}N [60, 77], Zn_xCd_{1-x}S [78, 79], CdS [73, 74, 80], CdS_vSe_{1-v} [81–83], CdSSe-CdS [84], CdSe [85, 86], GaAs [12, 56]), organic semiconductors (i.e. TPI [87], p-6P [88], DPBT [89], HBT [90], BP3T [91], 1d@2d [92], HDMAC [93], DMHP [94]), and inorganic-organic hybrid semiconductors (i.e. hybrid metal halide perovskites [95– 98]) have independently acted as gain media in NW lasers spectrally covering from the ultraviolet (UV) to near-infrared (NIR) regions. Engineering the bandgap energy would also tailor the operating wavelength of semiconductor NW lasers. For example, Qian et al. realized lasing spectrally from 382 to 484 nm in multi-quantum-well InGaN/ GaN core-shell NWs by varying the composition ratio of In [60]. Similar multicolor lasing has also been reported in composition-graded CdSSe and ZnCdS NWs [79, 81, 82]. Very recently, metal halide perovskites have shown considerable potential for multicolor lasers via tuning the content of the halogens, and all-inorganic alloying lead halide perovskites CsPb(Cl/Br), and CsPb(Br/I), NW lasers spectrally across the entire visible range have been reported at room temperature (Figure 1C) [72]. Moreover, white lasers obtained from a mixture of blue, green, and red light have also been demonstrated in a monolithic

ZnCdSSe nanosheet, strongly suggesting their potential for full-color display [99].

Propagating photons inside NWs inevitably suffer scattering from phonons, excitons, and impurities, causing significant energy shift to the emission colors. Even in undoped polar semiconductor NWs, excitonphonon coupling can induce additional electronic states inside the transparent bandgap and produce an exponential tail below the fundamental optical absorption edge [100-102]. This effect is known as the Urbach tail [103]. The propagating photons dissipate their energy gradually along the Urbach tail, giving rising to optical self-absorption, which reduces the intensity and frequency of the emission photons. More interestingly, the self-absorption effect also induces the red shift of the optical gain range, providing a pathway for multicolor lasing. For instance, Liu et al. tailored the lasing wavelength in CdS NWs by utilizing the self-absorption effect and demonstrated that the lasing wavelength could be shifted from 498 to 528 nm by increasing the CdS NW length from 4.3 to 16.4 µm (Figure 1D) [73]. A similar phenomenon was observed in CdSe NWs, which was identified as an absorption-emission-absorption process [104]. Meanwhile, under intense optical excitation, Fermi energy level in the conduction band may arise owing to the filling of the electronic states at the bottom of the conduction band, causing a blue shift to the emission, which is called as Burstein-Moss (BM) or band-filling effect [105, 106]. The energy shift induced by the BM shift is proportional to $n_0^{2/3}$, where n_0 is the electron carrier concentration in the conduction band and proportional to the pump fluence and inversely proportional to NW diameter. It means that the emission wavelength of NWs in both spontaneous emission and lasing processes can be modulated via tailoring the injection density or the NW diameter [107-110]. As demonstrated in a CdS NW/ SiO₂/Au photonic laser, the BM effect was dramatically enhanced by SP by increasing the local carrier concentrations, causing a 20-nm blue shift to the lasing wavelength on decreasing SiO₂ from 100 to 5 nm (Figure 1E, F) [74].

Moreover, with the rapid development in the fabrication of semiconductor NWs, highly ordered NW arrays have emerged, which hold great potential for highoutput, low-threshold laser sources. Vertically aligned NW arrays are mainly fabricated by template methods, microfabrication, and epitaxial growth such as molecular beam epitaxy (MBE), MOCVD, and pulsed laser deposition (PLD) [111–114]. Among these epitaxial routes, MBE can precisely control the height, composition, and structure of NWs at the sub-monolayer level; MOCVD exhibits fast and smooth growth, which is essential for mass

fabrications; and PLD combines the advantages of MBE and MOCVD, showing good compatibility with semiconductor technology. In addition, pretreating seeds or wetting layers are widely adopted to increase the density and improve the crystal quality of the NWs [115]. Up to now, vertical NW arrays of various semiconductors, especially Si and ZnO, have been fabricated with high yield (>97%) and large area (>1 cm²), wide size distribution (diameter: ~8-500 nm; height: ~1-100 µm), and various cross-sectional geometries [116–119]. Since the free spacing among NWs is much smaller than light wavelength, these NW arrays can not only support vertical F-P oscillations in a single NW but also trap emission along the horizontal direction of NWs so as to reduce scattering and realize electrically pumped random or/and edge-emitting lasing [13, 76, 113]. Owing to the collective contributions of NWs, these NW array lasers exhibit wide wavelength tunability (>15 nm), high coupling efficiency (>50%), high output power (~mW), and long working stability (>7000 h) in comparison to single NW lasers [13, 113, 120]. Electric field-assisted, flow-assisted, contact printing, bubbleblown, and Langmuir-Blodgett techniques have also been developed to guide the growth of in-plane aligned NW arrays [121-125]. Growth substrates with edge steps and V-grooves on the surface, such as Cu (110) [126], sapphire $(10\overline{1}0)$ [57], GaAs (100) [127], and muscovite mica (100) [59], have also been used for the growth of in-plane NW arrays. To date, a wide range of in-plane NW arrays have been synthesized, from III-V (GaN, GaAs, InP, InAs), II-VI (ZnO, ZnSe, CdS), and IV (Si, Ge) group semiconductors to the recent lead halide perovskite [57, 59, 121-125, 127-130]. These NW array lasers exhibit identical lasing threshold and color from independent sub-units, and can be compatible with lithography techniques and integrated circuits; for example, the InP NW array lasers realized the complex spatial patterns for flat panel display [98, 131]. These excellent capabilities on high-power and ordered lasers make NW arrays an important branch of semiconductor NW lasers.

3 Introduction to surface plasmon

SPs were first predicted and confirmed through electron energy loss experiments in the 1950s [19]. Compared with purely longitudinal bulk plasmons, SPs have both transverse and longitudinal electric field components, creating opportunities to confine light into sub-wavelength volumes. SP polariton (SPP) quantizes a surface propagating wave along the metal-dielectric interface but an

evanescent wave in the direction perpendicular to the interface. Considering a single flat interface of metal layer (dielectric function: $\varepsilon_{\rm m}(\omega) = \varepsilon_{\rm m}'(\omega) + i\varepsilon_{\rm m}''(\omega)$) beneath dielectric layer (dielectric function ε_d), the dispersion curve of the SPP is expressed as $k_{\rm SPP} = \frac{\omega\sqrt{\varepsilon_d}}{c}\sqrt{\frac{\varepsilon_{\rm m}}{\varepsilon_{\rm m}+\varepsilon_{\rm d}}}$, where $k_{\rm spp}$ is the wave vector of SPP, and ω , c are the in-plane

angular frequency and speed of light in vacuum, respectively. Since the dispersion curve is always on right side of photons, SPP has a larger wave vector than light in free space, and therefore cannot be directly excited by illumination from the dielectric layer. Meanwhile, due to ohmic losses of the metal by free-electron scattering and interband absorption, SPPs are inevitably damped during their travel. For example, the theoretical propagation length of SPPs at an Ag-air interface, which is the distance when their intensity decays by a factor of 1/e, is over 20 μ m at $\lambda = 510$ nm and even 10^3 µm at $\lambda = 1500$ nm. In contrast, the skin depth of SPPs at optical frequencies is typically on the order of 10 nm in metal and 10² nm in the dielectric layer, indicating a strong localized electromagnetic field near the interface.

On the other hand, localized excitation can exist in bounded geometries, such as metal nanoparticles, which is called localized SP (LSP) [132]. The origin of LSP can be explained by the interaction of a spherical metal nanoparticle with an oscillating electromagnetic wave, in which the curved surface of metal nanoparticle exerts a restoring force on the driven oscillating electric field to form a resonance [133]. Given that the radius of the metal nanoparticle is much smaller than light wavelength, the frequency of LSP resonance can be decided by using a quasi-static approximation. The as-applied electric field induces a dipole moment inside the metal nanoparticle, and the polarizability experiences a resonance enhancement as $\varepsilon_{\rm m}' = -2\varepsilon_{\rm d}$ (Fröhlich criterion). For a Drude metal in air, the Fröhlich condition will be satisfied at the resonance frequency of $\omega_n/\sqrt{3}$, where $\omega_{\rm p}$ is the frequency of the free-electron plasma. Correspondingly, the field enhancement at the metal surface is described as $|3\varepsilon_m/\varepsilon_m''|^2$, which can reach over 450 at $\lambda = 350$ nm for a Ag nanosphere as an example. Similarly, anisotropic metal nanoparticles with high aspect ratio and low depolarization factor are considered to have a high theoretical enhancement factor (e.g. 105 for a Ag nanospheroid with aspect ratio 3). It suggests that, apart from the size and the dielectric function of the surrounding environment, the geometry and shape of metal nanoparticles also significantly influence the resonance frequency and local field enhancement factor of the LSP [134].

Although SPP and LSP differ significantly in many properties, they are still closely interlinked. At large k_{spp} $(\varepsilon_{\rm m} + \varepsilon_{\rm d} \rightarrow 0)$, e.g. ω approaches the SP frequency, and the group velocity is approximately zero for an undamped plasmon. It suggests that SPPs are strongly concentrated around the metal-dielectric interface with almost disappearing propagation behaviors, which is analogous to the LSP. Moreover, SPP and LSP can excite each other on a rough surface as their frequencies are close. Since LSP can be easily excited by photons with comparable frequency and polarization, this provides a strategy to excite SPP via roughness coupling without satisfying the wave vector matching condition.

Fundamental and application studies on SP have been rapidly developed in the past. First, SP-induced field localization and enhancement have been widely used to amplify weak and strong light-matter interactions, such as surface-enhanced Raman scattering (SERS), surface-enhanced fluorescence, surface-enhanced nonlinear processes, and so on [135]. The enhancement factors of SERS have reached 107-1010, or even 1014-1015. making it possible to detect chemical and biological samples at the single-molecule level [136–138]. Second, LSP resonance frequency is sensitive to the surrounding environment, which is applied in sensors, displays, photothermal devices, and so on [139-141]. By probing the LSP resonance of Au nanodisk arrays close to catalyst Pt nanoparticles, Larsson et al. monitored the real-time dynamics of H₂ oxidation, CO oxidation, and the storage and reduction of NO₂ with sensitivity of 10⁻³ monolayer molecule [142]. Using a similar method, the intraparticle distance between single-stranded DNA-functionalized metal nanoparticle pairs upon DNA hybridization was determined with detectable separations of up to 70 nm for >3000 s, which is much better than the molecule rule using Förster resonance energy transfer, suggesting the potential of SPs for bioimaging and cancer treatment [143]. Owing to the strong spatial confinement and longrange propagation, SPP waveguides, including wedge, groove, metal cylinder, MIM, and MISW, are designed to construct integrated nanocircuits [15]. For example, networks of Ag NWs were fabricated to realize all-binary logic functions including AND, OR, and NOT by controlling the polarization and phase of the input light [144]. Also, combing SPs with metamaterials has exploited a revolutionary field to tailor light behavior in a way that does not exist in natural materials, ranging from negative refraction, hyperbolic dispersion, epsilon-near-zero, transformation optics, and invisibility cloak to subwavelength imaging, which motivate new exciting applications of SPs [145-147].

4 Plasmonic nanowire lasers: from theory to experiment

On the concept of the plasmonic laser, SPs are amplified via stimulated emission of excitons generated in a semiconductor gain medium. The energy of excitons is transferred to the metal nonradiatively to excite one SP, and moves back to stimulate the exciton for cycling to create more SPs. In a plasmonic NW laser, excitons strongly couple with SPs to form coherent long-range SPP (LRSPP) waves, which propagate along the metal-semiconductor interface and get reflected at the two end-facets of the NW [148-150]. LRSPP wave decoupling at the end-facets can radiate photons into free space, showing lasing characteristics when the optical gain is larger than the optical losses. According to Maxwell's equations, the wavelength of SPP is always smaller than that of photon for a fixed frequency, so the formation of LRSPP includes near-field momentum exchange and below-diffraction-wavelength compression.

In 2008, Oulton et al. proposed a hybrid plasmonic waveguide including a semiconductor NW with high refractive index, a metal film, and a sandwiched nanometer-sized insulator layer with low refractive index, which has become one of the most popular configurations for plasmonic lasers (Figure 2A) [151]. As shown in Figure 2B, as the insulator layer thickness was 100 nm, the hybrid photonic mode was predominant and resulted in the electromagnetic field mostly distributed inside the 400-nm GaAs NW. However, as the thickness of the insulator layer was reduced to 2 nm, the hybrid plasmonic mode was strongly confined within the interface region owing to the continuity of the displacement field (Figure 2B), and the mode area ranged from $\lambda^2/40$ to $\lambda^2/400$. The effective refractive index was larger than that in a pure dielectric waveguide, leading to better optical confinement. Since

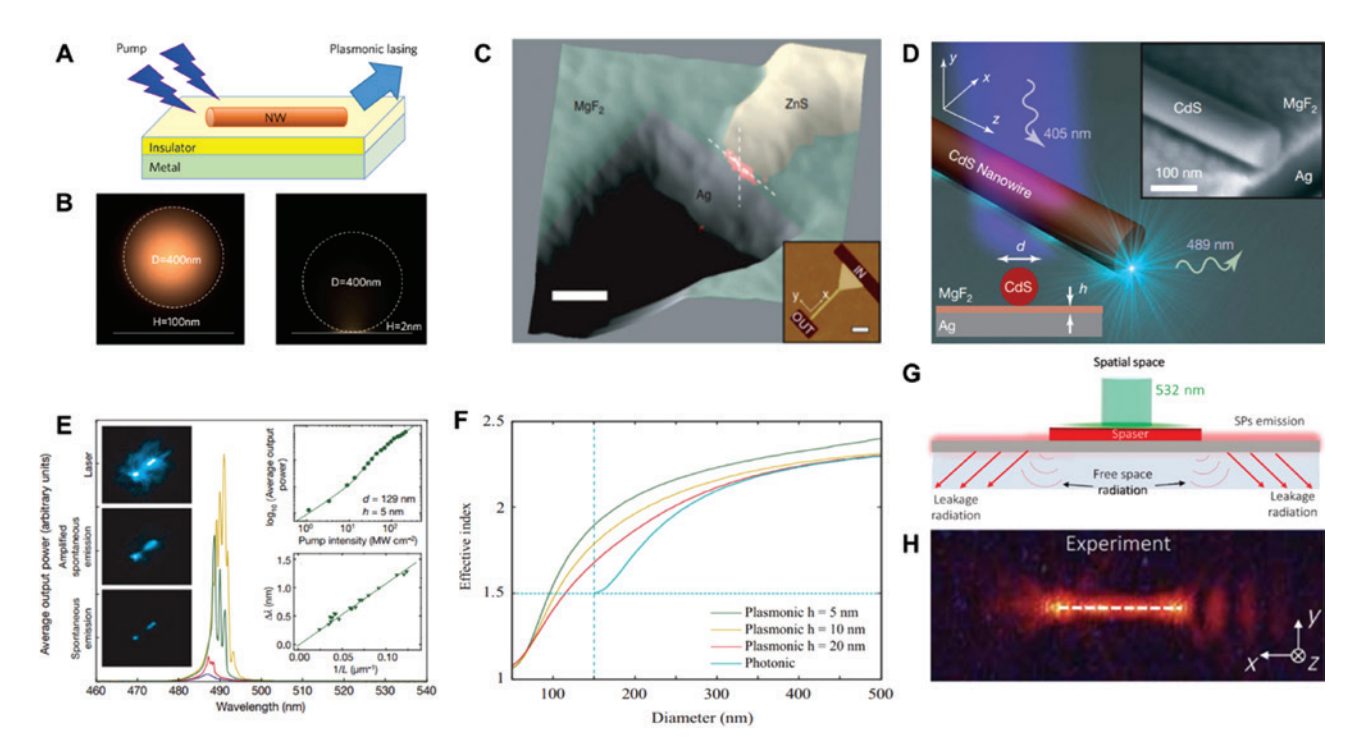


Figure 2: Demonstration of a plasmonic NW laser.

(A) Schematic of a semiconductor waveguide-insulator-metal film nanocavity for plasmonic lasing. (B) Electromagnetic energy density distributions of a 400-nm-diameter GaAs NW sitting on Ag film with SiO, spacing. SiO, thickness: 100 nm (left) and 2 nm (right). Reproduced with permission [151]. Copyright 2008, Springer Nature. (C) Three-dimensional image overlap of near-field electromagnetic intensity of ZnS/MgF,/Ag. The gap area (red spot) shows the sub-wavelength optical confinement. Inset: height profile of tapered strip. Reproduced with permission [152]. Copyright 2011, Springer Nature. (D) Schematic of a plasmonic laser based on CdS NW/MgF,/Ag. Inset: Scanning electron microscope image of the hybrid structure. (E) Spectra for different pump intensities exemplifying the lasing action in the plasmonic device. Insets: microscope images of the plasmonic laser at spontaneous emission, amplified spontaneous emission, and laser oscillation; the output power versus pump intensity and mode spacing versus NW length. (F) The effective mode indexes of hybrid plasmonic modes and photonic mode as a function of the NW diameter. Reproduced with permission [31]. Copyright 2009, Springer Nature. (G) Schematic of leakage radiation microscopy for imaging emission of plasmonic NW lasers. (H) Spatial image of one plasmonic NW laser emission. Reproduced with permission [153]. Copyright 2017, American Association for the Advancement of Science.

the electromagnetic field was mostly distributed inside the low-loss insulator layer, the propagation distance was as large as ~23.07 λ . Existence of the hybrid plasmonic mode was then demonstrated by Sorger et al. in a ZnS strip (thickness: 200 nm, width: 150-800 nm) placed on a Ag film separated with a MgF, layer (thickness: 10 nm) [152]. As shown in Figure 2C (inset), the strip was excited by light illumination at one end of a metal slit, and the local electromagnetic field intensity of the opposite end was detected by a near-field scanning optical microscopy tip. A strong local electric field was observed at the insulator region with a vertical dimension of ~50 nm, which was far below the diffraction limit of light and in good agreement with the theory.

In 2009, Oulton and coworkers demonstrated deepsub-wavelength plasmonic mode lasing from a glossy single-crystalline CdS NW on top of a silver film with a nanometer-thick MgF, insulator layer (Figure 2D) [31]. The plasmonic device was optically pumped by a femtosecond pulsed laser (405 nm, 100 fs) below 10 K. Figure 2E exemplifies the transition from spontaneous emission (21.25 MW cm⁻²) via amplified spontaneous emission (32.50 MW cm⁻²) to full laser oscillation (76.25 and 131.25 MW cm⁻²) of the plasmonic laser. The log-log scale plot of the output power versus the pump intensity showed an "S"-like curve, which could be well fitted by a rate equation (inset, Figure 2E). Moreover, the free spectral range of these modes showed a linear relationship with the reciprocal of the NW length, confirming the F-P oscillation of the NW laser (inset, Figure 2E). The effective refractive indexes of the hybrid plasmonic and photonic mode as a function of NW diameter, shown in Figure 2F, revealed that the photonic mode was cut off below 140 nm while the plasmonic mode was not limited in the region of interest. As a result, lasing of NWs with diameter less than 140 nm could be derived only from the plasmonic mode. Although the threshold of plasmonic lasers (~100 MW cm⁻²) was still higher than that of dielectric lasers, facile excitation condition of the first plasmonic NW laser showed broad potential for sub-wavelength coherent sources. Thereafter, hybrid plasmonic NW lasers have been implemented in demonstrations for InGaN/GaN (~474-627 nm) [154], GaN (~375 nm) [155], GaAs/AlGaAs (~804 nm) [156], ZnO (~380 nm) [157–159], CdS (~486 nm) [160], and CsPbBr₃ (~526 nm) [161], as listed in Table 1.

In 2017, Chen et al. demonstrated a Ag-SiO₂-CdSe NW plasmonic laser and directly imaged the spatial distribution of plasmonic lasing by using a leakage radiation microscope (Figure 2G) [153]. In their experiments, the emission coupled to the SP mode could be collected at a certain polar angle satisfying the momentum matching condition. Figure 2H shows the spatial image of a plasmonic NW laser with the diameter of 212 nm and the length of 8.4 μm. Pronounced emission was observed mainly along the NW long axis, which was attributed to the fundamental plasmonic mode rather than the photonic mode. Moreover, the generation efficiency of SPs, defined as the power ratio of SP emission to the total emission, was as high as 74%, which was expected to be ~100% in NWs with diameter less than 50 nm. These results proved the promise of radiating SPs

Table 1: Key metrics of representative plasmonic NW lasers.

Year	Gain medium	Size	Insulator-metal	Wavelength (nm)	Pump	Temperature	Threshold	Reference
2009	CdS	Diameter: ~100 nm Length: ~10 μm	MgF ₂ -Ag	489	Optical, pulsed	<10 K	~100 MW cm ⁻²	[31]
2012	InGaN/GaN	Diameter: ~60 nm Length: ~480 nm	SiO ₂ -Ag	510	Optical, CW	78 K	~3.7 kW cm ⁻²	[154]
2014	GaN	Diameter: ~100 nm Length: ~15 μm	SiO ₂ -Al	375	Optical, pulsed	RT	~3.5 MW cm ⁻²	[155]
2015	GaAs/AlGaAs	Diameter: ~150 nm Length: ~5 μm	Non-Ag	804	Optical, pulsed	8 K	~1 kW cm ⁻²	[156]
2016	ZnO	Diameter: ~150 nm Length: ~1.7 μm	Non-Al	380	Optical, pulsed	300 K	~105 MW cm ⁻²	[157]
2017	ZnO	Diameter: ~150 nm Length: ~7 μm	MgF ₂ -Ag	380	Optical, pulsed	RT	\sim 1.69 GW cm $^{-2}$	[159]
2017	CdS	Diameter: ~115 nm Length: ~12 μm	SiO ₂ -Ag	486	Optical, pulsed	77 K	\sim 75 μ J cm $^{-2}$	[160]
2018	CsPbBr ₃	Diameter: ~120 nm Length: ~2.8 μm	SiO ₂ -Ag	526	Optical, pulsed	RT	~6.5 µJ cm ⁻²	[161]

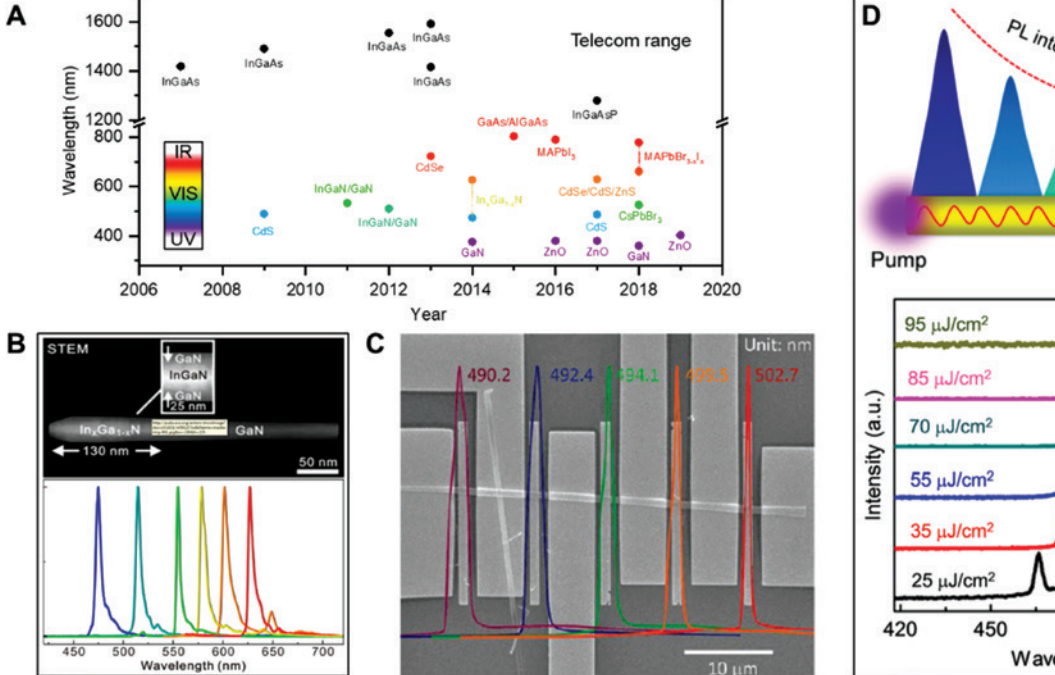
RT, Room temperature; CW, continuous wave.

in various applications from on-chip integration, nonlinear photonics, and imaging to sensing. Nevertheless, the exploration of plasmonic NW lasers is not limited to these observations of lasing actions, but also needs more effort to uncover the underlying photophysics and improve the lasing performance toward next-generation nanoscale light sources. Next, we will introduce the progress in plasmonic NW lasers from the aspects of color tuning, lowthreshold, high-speed modulation, electrically pumped devices, and relevant applications.

5 Multicolor plasmonic lasers

The realization of multicolor lasers is important for satisfying diverse applications such as illumination, display, communication, and sensors [162-166]. Since the operation band of lasers mainly depends on the electronic bandgap of the gain media and the SP frequency, plasmonic lasers working in the spectral range from UV to NIR have been established by using semiconductor materials

of different gains (Figure 3A) [31, 32, 154-157, 159-161, 167, 169–179]. A strategy is using multiple compounds of semiconductor gain media and controlling their elemental composition during fabrication processes. For example, Lu et al. have reported a single-mode, all-color, continuous wave (CW), deep-subwavelength plasmonic laser operated at 7 K. The nanocavity included InGaN/ GaN core-shell nanorods (diameter: ~30-50 nm, length: 100–250 nm) sitting on a 28-nm Ag film with a 5-nm Al₂O₃ film as the separating layer (Figure 3B) [167]. By tuning the content ratio of In from ~27% to 53%, the electronic bandgap could be varied from ~2.65 to 1.93 eV, leading to the plasmonic lasing of 474–627 nm. Another strategy is to vary the dimension and morphology of the plasmonic nanocavity, such as the width and the length of semiconductors, and the substrate type. Ma et al. have demonstrated a room-temperature, multicolor plasmonic laser from a single CdS nanobelt (width: ~620 nm, thickness: 100 nm), which was crosswise integrated onto five silver strips (width: 1 µm, thickness: 250 nm) separated by a 5-nm MgF, gap [168]. Six In/Au (10/120 nm) ohmic contact



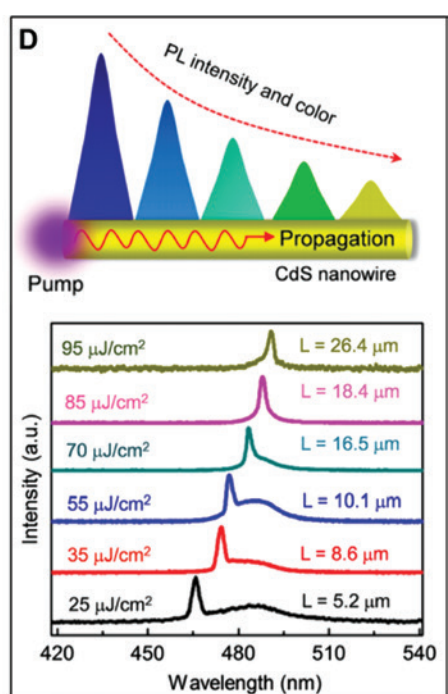


Figure 3: Wavelength-tunable plasmonic NW lasers.

(A) Development of various devices working in the spectral range from UV to NIR. (B) Top: scanning transmission electron microscopy image of an InGaN/GaN core-shell nanorod. Bottom: spectra of single-mode lasing actions from 474 to 627 nm. Reproduced with permission [167]. Copyright 2014, American Chemical Society. (C) Scanning electron microscope image of a plasmonic device including five plasmonic lasers assembled from CdS strips crossing five silver strips and the emission wavelength modulated from 490.2 to 502.7 nm. Reproduced with permission [168]. Copyright 2012, American Chemical Society. (D) Top: schematic of the emission intensity and color change during the propagation of emission light in plasmonic CdS/SiO₃/Ag device. Bottom: lasing peak wavelength tailored in different lengths of CdS NWs owing to self-absorption. Reproduced with permission [160]. Copyright 2017, American Chemical Society.

electrodes were constructed to provide additional electrical modulation, as shown in Figure 3C. When the overlap areas of Ag and CdS were optically pumped, a hybrid plasmonic mode was supported along the metal-dielectric interface, and the lasing wavelength spanned from 490.2 to 502.7 nm by varying the width of the CdS waveguide. In addition, when an electric field was applied (4 V), a small linear peak shift (below 0.3 nm) was achieved as a result of the enhanced density of excited carriers, providing a solution to tailor the wavelength precisely and dynamically. More than 70% of the plasmonic energy could be guided into the embedded CdS waveguide with thickness >60 nm, and the radiation efficiency was also remarkably enhanced by ~35%. As shown in Figure 3D, Zhang et al. reported that the operation wavelength of Ag-SiO₂-CdS NW plasmonic laser shifted from 465 to 491 nm as the CdS NW length was increased from 5.2 to 26.4 µm, which covered approximately 76% over the interval width of the emission spectrum of CdS [160]. The plasmonic mode was always located on the high-energy side of the spontaneous emission peak owing to the BM effect, which is further enhanced and tuned by the SPPs in the nanocavity. Also, the red shift of lasing modes caused by the self-absorption effect of the semiconductor is sensitive to the diameter of NWs, e.g. a larger diameter gives rise to a larger shift [73]. These methods of tuning the lasing wavelength can be easily extended to other semiconductor NW plasmonic lasers.

6 Low-threshold plasmonic lasers

Reducing mode losses and harnessing optical gain are two strategies to achieve low-threshold plasmonic NW lasing. The large loss in a plasmonic cavity is mainly contributed by four parts: (1) free-electron scattering with electrons, lattice ions, and impurities at the damping rate of $\sim 10^{-15}$ s⁻¹ [180]; (2) intra/interband transition for excitation of electron-hole pairs, which is dependent on the optical wavelength, e.g. for Au and Ag, the intraband and interband losses are high in the NIR and visible region [145, 181]; (3) scattering into LSP or free-space radiation within the time scale of 10 fs [182]; (4) radiation loss occurring primarily at cavity interface, i.e. end-facets for NW, which is relatively low compared to the other three channels in plasmonic lasers. The total loss is on the order of 10³ cm⁻¹, which can only be overcompensated by the optical gain from semiconductors with a carrier concentration of ~10¹⁹ cm⁻³. To promote optical gain and compensate optical losses, large gain-mode overlap and rapid exciton-plasmon energy

transition rate are necessary, which are dependent on the morphology of the semiconductor, metal, and their interfaces [183]. To date, in order to reduce the threshold of plasmonic lasing, interface engineering, rational selection of metal and semiconductor materials, as well as nanocavity designs have been proposed.

As shown in Figure 4A, Lu et al. have demonstrated a CW pumped MISW plasmonic laser using InGaN/GaN core-shell nanorod as the gain medium, Ag film (28 nm) as the metal layer, and SiO, film (5 nm) as the insulator layer [154]. Both the mode volume and losses were effectively reduced by adopting an MBE-grown, atomically flat Ag film. The lasing threshold was as low as 3.7 kW cm⁻² at 78 K. Similarly, Chou et al. successfully boosted the performance of a UV plasmonic nanolaser by utilizing a glossy single-crystalline Al film with a root-mean-square roughness of 0.44 nm (Figure 4B) [184]. The lasing threshold was dramatically reduced to 0.28 mJ cm⁻², which was 36 times lower than that of the device using polycrystalline Al film with a roughness of 2.29 nm (Figure 4B). These works tell us that small roughness of the metal surface and the interface is important issue for low-threshold plasmonic NW lasers.

In 2014, Zhang et al. realized a room-temperature, single-mode UV plasmonic laser with a low threshold of 3.5 MW cm⁻² by adopting GaN NWs with triangular cross-sections (Figure 4C) [155]. In this work, the core technology was to construct the closed-contact, planar metal-semiconductor interface to suppress interface scattering losses and promote exciton-plasmon interaction. Later, Chou et al. reported a single-mode ZnO NW plasmonic laser operating at 353 K, and found that the threshold was even lower without the insulator layer owing to the relatively strong confinement (Figure 4D) [157]. The authors also confirmed that the SPP mode field was well confined for the Al-ZnO configuration.

Furthermore, the plasmonic lasing threshold is also highly dependent on the dimension of the nanocavity. Wang et al. have explored the scaling laws of threshold versus the cavity size in a Au-MgF₂-CdS MISW plasmonic laser (Figure 4E) [185]. As the thickness of the CdS nanosquares was 100-200 nm, the threshold of both plasmonic and photonic lasers increased with the decrease of the cavity volume owing to the reduction of mode overlap and cavity quality factor. As the thickness was <100 nm, a similar trend was observed in plasmonic devices (inset, Figure 4E). These results indicated that the size of nanocavity should be as large as possible to decrease the lasing threshold. On the other hand, an enhanced spontaneous emission factor is predicted in a smaller mode volume, which can increase the coupling between excitons

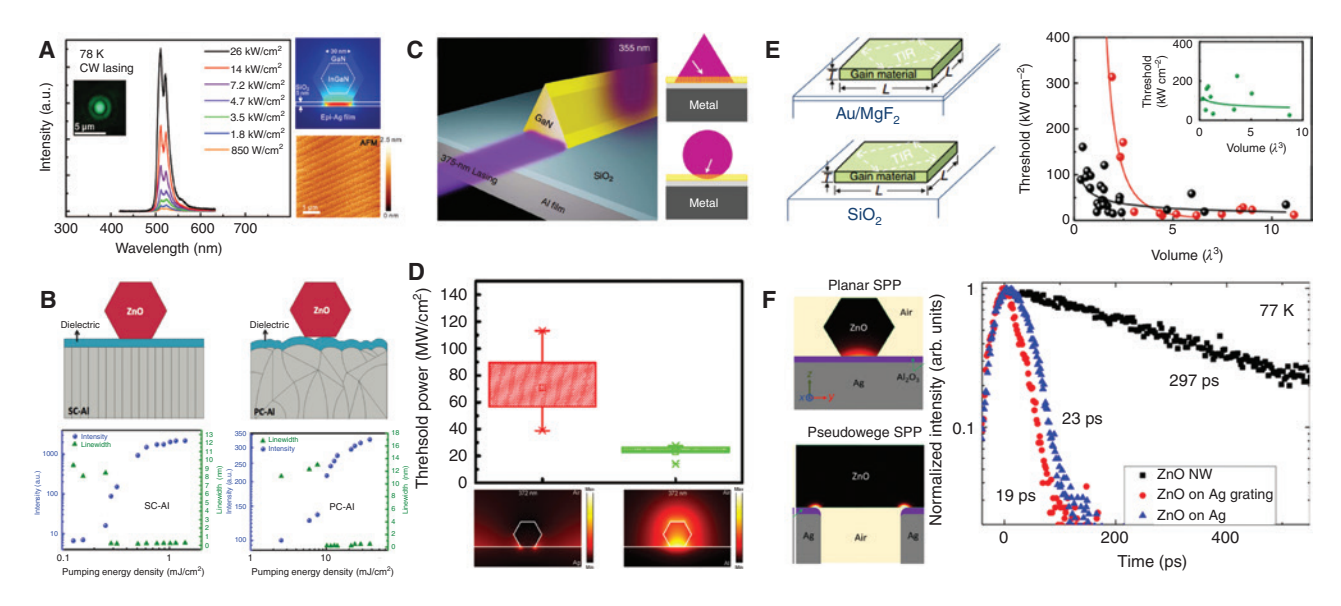


Figure 4: Threshold reduction in plasmonic NW lasers.

(A) Left: lasing spectra of the InGaN@GaN/SiO₂/Ag device pumped by a CW 405 nm laser. Inset: the far-field laser spot. Right: energy-density distribution in the plasmonic nanolaser and atomic force microscopy (AFM) image showing that Ge-capped Ag film remains atomically smooth in air. Reproduced with permission [154]. Copyright 2012, American Association for the Advancement of Science. (B) Top: schematic of the ZnO NWs on the tops of the single-crystalline and polycrystalline Al films with a dielectric spacer layer. Bottom: emission intensity and line width as functions of the pumping fluence in the two devices. Reproduced with permission [184]. Copyright 2016, Springer Nature. (C) Left: schematic of the GaN NW/SiO₂/Ag device. Right: effective gain area (yellow area) in two types of semiconductor-insulator-metal interface. Reproduced with permission [155]. Copyright 2014, Springer Nature. (D) Top: average threshold comparison for ZnO/Al and ZnO/Al₂O₃/Al nanolasers. Bottom: calculated electric field profiles of ZnO/Ag and ZnO/Al structures for 372 nm. Reproduced with permission [157]. Copyright 2016, American Chemical Society. (E) Left: schematic of plasmonic laser (CdS/MgF₂/Au) and photonic laser (CdS/SiO₂). Right: laser threshold versus device volume for plasmonic (black dots) and photonic (red dots) nanolasers with thicknesses in the range 100–150 nm. Inset: laser threshold versus device volume for plasmonic nanolasers with thicknesses below 100 nm. Reproduced with permission [185]. Copyright 2017, Springer Nature. (F) Left: simulated local Purcell factors of planar and pseudo-wedge SPP nanolasers. Right: carrier dynamics of ZnO NWs on flat Ag and Ag gratings at 77 K. Reproduced with permission [186]. Copyright 2018, American Chemical Society.

and cavity modes to decrease the lasing threshold. For example, Chou et al. demonstrated a single-mode, pseudowedge plasmonic laser with a threshold of ~50 MW cm $^{-2}$ [186]. The effective mode volume in this device was only 0.000015 λ^3 , which was 100 times smaller than that of a planar SPP laser, leading to enhanced Purcell effect and shortened photoluminescence decay time (Figure 4F). As a result, a high spontaneous emission factor of ~0.8 was achieved at the intersections between ZnO NWs and Ag gratings, suggesting a pathway for low-threshold plasmonic lasing with reduced dimensions.

7 Ultrafast modulation

Fast response of lasing devices is important for on-chip data transport and optical computation. To date, subpicosecond switching time is realized in various structures including interferometry structures, nonlinear fibers, waveguides, and semiconductor optical amplifiers

[187]. The ultrafast dynamics, as predicted by pioneering theoretical works on SPs, is mainly attributed to the accelerated recombination rate induced by enhanced mode confinement, which is the so-called Purcell effect [188]. In 1946, Purcell effect was primarily proposed to ascribe the rate acceleration of the spontaneous radiation of oscillators in optical cavities [189]. Compared to freespace emission, the density of states increases when the oscillators are coupled to microcavity modes (Figure 5A), and the recombination rates of oscillators are enhanced by a factor expressed as $F_{\text{purcell}} = \frac{3}{4\pi^2} \left(\frac{\lambda}{n}\right)^3 \frac{Q}{V_{\text{m}}}$, where V_{m} and Q represent the cavity volume and quality factor, respectively [192–194]. As such, both increasing Q and decreasing V_{m} can promote F_{Purcell} , and SPs provide a great platform to increase $F_{Purcell}$ and enhance the emission rate by their strong confinement. For instance, in a micropillar photonic laser, F_{Purcell} was only 10 when Q was ~16,000, but it increased to 18 in a CdS nanosquare plasmonic laser despite the fact that Q was only ~100 [195, 196]. Meanwhile, the as-reported $F_{\mbox{\tiny Purcell}}$ of ZnO NW UV plasmonic

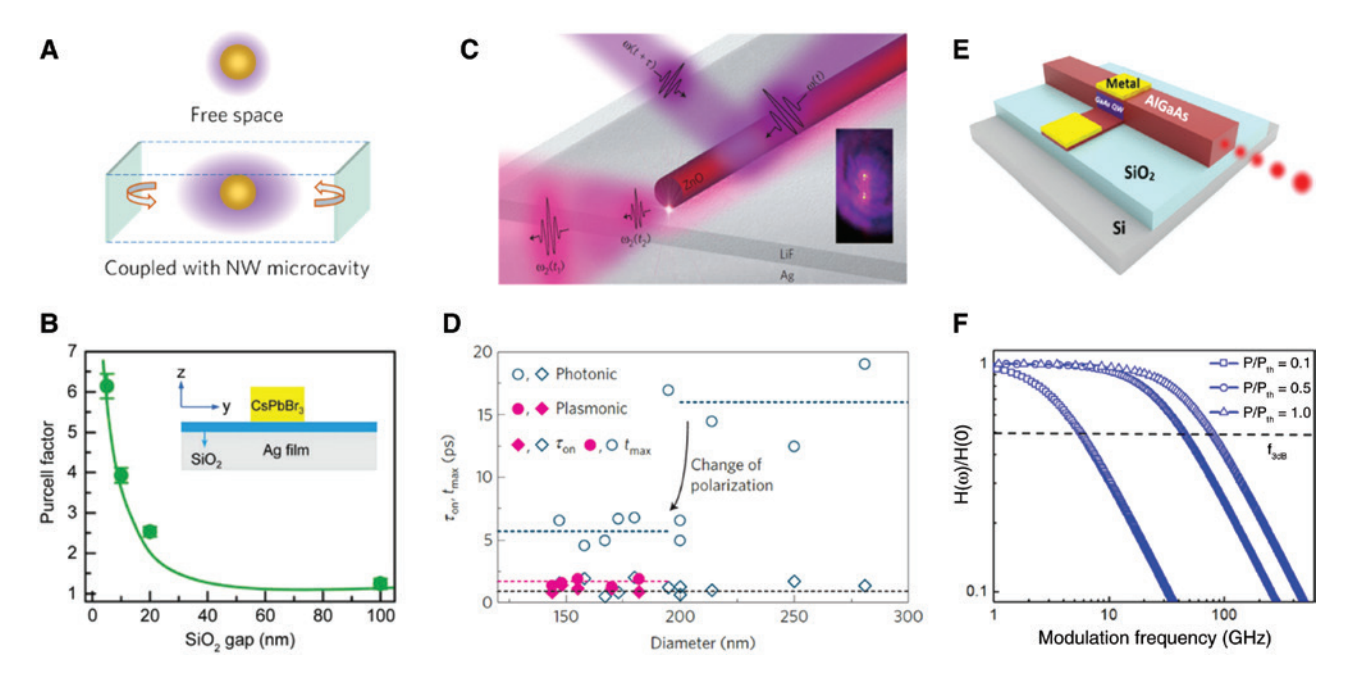


Figure 5: High-speed modulation of plasmonic NW lasers. (A) Schematic of the Purcell effect in the NW nanocavity. (B) Purcell factor as a function of SiO, thickness for the CsPbBr, NW/SiO,/Ag devices, Inset: schematic of the plasmonic nanolaser, Reproduced with permission [161], Copyright 2018, Wiley-VCH. (C) Schematic of the plasmonic laser based on ZnO NW/LiF/Ag optically excited with two time-delayed pump pulses. Inset: optical image of a lasing plasmonic NW. (D) Characteristic temporal parameters τ_{on} (diamonds) and t_{max} (circles) for the same plasmonic (closed symbols) and photonic (open symbols) NWs. Reproduced with permission [190]. Copyright 2014, Springer Nature. (E) Schematic of inline plasmonic cavity-based nanolaser. (F) Modulation bandwidth of the inline cavity nanolaser/LED at different pump rates. Reproduced with permission [191]. Copyright 2016, American Chemical Society.

lasers, by Chou et al., and Lu et al., reached 20.4 and 40 [158, 197]. Recently, in a plasmonic laser adopting emergent CsPbBr, perovskite as the gain medium, Wu et al. demonstrated that the radiative recombination lifetime of the perovskite NWs was shortened by a factor of ~6.14 due to Purcell effect (Figure 5B) [161]. The high $F_{\text{\tiny Purcell}}$ suggests a fast response of plasmonic lasers. In 2014, Sidiropoulos et al. used a pump-probe method to measure the response time of plasmonic and photonic lasers, respectively [190]. As shown in Figure 5C, individual ZnO NWs were placed on a 10-nm-thick LiF layer over Ag substrate to form an MISW structure, which was then sequentially excited by a high-energy pulse above the threshold (200 µJ cm⁻²) and a low-energy pulse below the threshold with a delay time. The time delays between the input and output pulses were measured as t_1 for the high-energy pulses and t_2 for lowenergy pulses. As shown in Figure 5D, since the population inversion was mainly created by the initial pulse, the opening time of the plasmonic laser, approximately equal to t_1 , was ~1 ps. The corresponding pulse line width was 0.8 ps, which was nearly one order of magnitude smaller than that of the photonic laser (4-5 ps). The average response time when the intensity of stimulated emission reached a maximum value was only 1.6 ps for the

plasmonic laser, which was much shorter than that of the photonic laser (5.7 ps).

Modulation bandwidth of a laser, f_{3dB} , which represents the frequency when its response function drops to half the initial value, is another important factor to characterize the response rate of lasers. Under low pump intensity such as far below the lasing threshold, $f_{\rm 3dB}$ is mainly limited by the relaxation rate of the emitters, theoretically proportional to $\sqrt{F_{\text{Purcell}}\gamma}$, and increases with F_{Purcell} and the cavity loss γ . As the pump intensity is far above the lasing threshold, an upper bandwidth limit of f_{3dB} is determined by the cavity loss γ . Both F_{purcell} and γ of plasmonic cavities are quite high, leading to a large f_{AB} for plasmonic lasers. For example, Genov et al. predicted terahertz bandwidth from one-dimensional Ag NW plasmonic waveguide in the mid-IR spectral range (1550 nm) owing to the strong mode confinement, suggesting the great potential of plasmonic NW lasers for wide-band telecom applications [198]. As shown in Figure 5E, Liu et al. designed an electrically pumped one-dimensional plasmonic laser with $F_{Purcell} = 10$ using GaAs quantum wells as the gain medium [191]. $f_{\rm 3dB}$ was ~80 GHz at the lasing threshold of ~3000 kA cm⁻², which exceeded the classical on-chip sources by a factor of more than two (Figure 5F). Moreover, the plasmonic

laser exhibited a high coupling efficiency of >60% to a planar AlGaAs waveguide on a silicon-on-insulator (SOI) substrate, promising for on-chip ultrafast laser sources.

8 Electrically driven plasmonic lasers

Optical and electric pumping are the most popular routes to realize population inversion of a gain medium. Most of the as-introduced lasers in the previous paragraphs are pumped by femtosecond pulsed lasers, which are still far from practical applications. Electrically injected operation is central for applications of plasmonic lasers, but it still faces considerable challenges and has been a longstanding problem [199]. The large ohmic losses and joule heating of electrical injection drastically reduce the effective gain and increase the operation threshold. Typical amplitude of electrical density for electrically driven plasmonic lasers is over ~70 A cm⁻², which is nearly one

order of magnitude larger than that of photonic microlasers. The crystalline structure of semiconductors as well as their emission spectra may change under such a high injection condition, hampering the stability and reliability of plasmonic lasers [200].

Hill et al., in 2007, initially demonstrated an electrically driven, metal-cladded NW laser, which was indeed above the optical diffraction limit but still became a popular settlement to compress the laser dimension to the sub-wavelength range [201]. In 2009, Hill et al. completed the first electrically driven plasmonic laser composed of a rectangular cross-section n-InP/InGaAs/ p-InP pillar (InGaAs height: 300 nm), which was surrounded by an insulating SiN layer (thickness: 20 nm) and further encapsulated by Ag films, as shown in Figure 6A [32]. Therein, the InGaAs in the core region acted as the gain medium and was excited by two Au/ Pt/Ti electrical contacts, and the n-InGaAs/n-InP and p-InGaAs/p-InP functioned as electron and hole injection layers, respectively. Owing to the dielectric contrast between the InGaAs and InP layers, the SPP mode

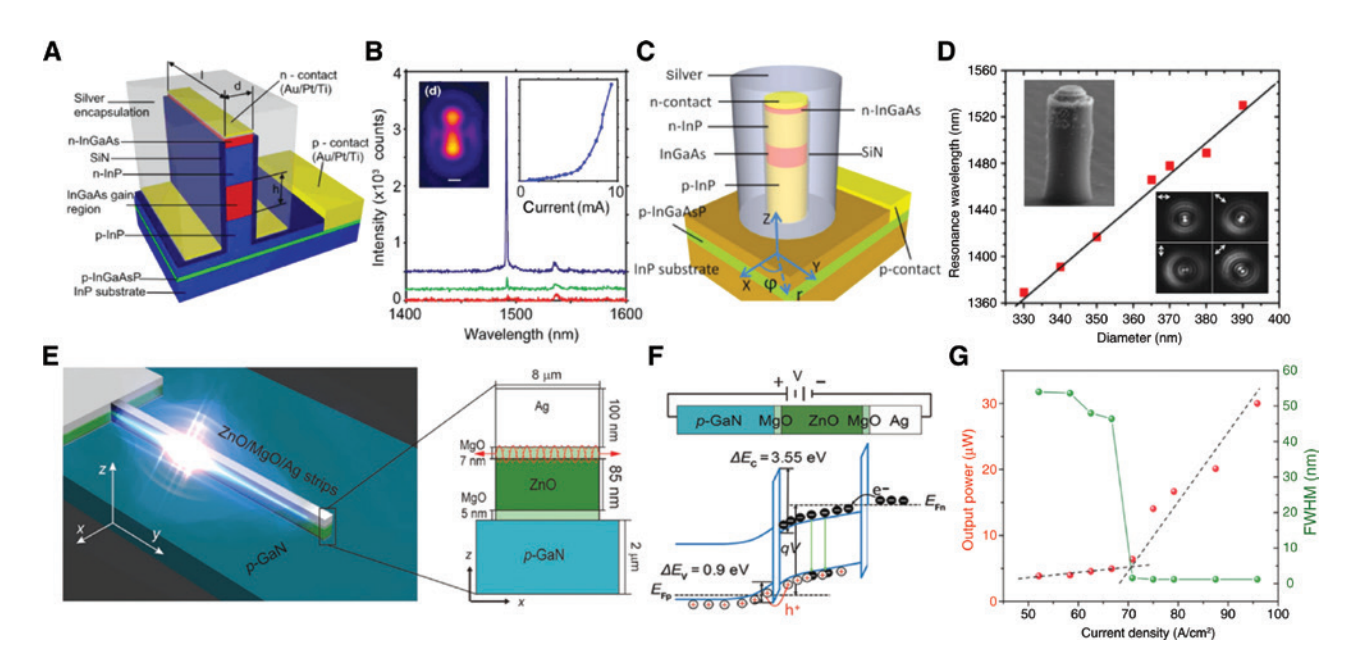


Figure 6: Electrically driven plasmonic NW lasers.

(A) Schematic of an electrically injected plasmonic laser formed by a rectangular n-InP/InGaAs/p-InP pillar encapsulated in silver separated by SiN. (B) Spectra for injection currents of 5.2 mA (red), 5.9 mA (green), and 7.4 mA (blue) in a 6-µm-long device at 298 K. Insets: nearfield pattern of the device above the threshold and the total light output versus current from 0 to 10 mA. Reproduced with permission [32]. Copyright 2009, The Optical Society. (C) Schematic of an electrical injection metallic nanolaser, where the core-shell structure is cylindrical. (D) Linear dependence of the emission wavelength on diameter over 160 nm. Insets: Scanning electron microscope image of the device and four output images taken by an NIR camera behind a linear polarizer in different orientations, confirming the azimuthal polarization of the plasmonic laser. Reproduced with permission [172]. Copyright 2013, American Institute of Physics. (E) Schematic of a room-temperature, electrically driven UV plasmonic laser. Inset: structure of the hybrid device, where the layer stack (from top to bottom) is Ag/MgO/ZnO/ MgO/GaN. (F) Schematic of the energy band structure in the device. (G) Output power and line width of the lasing peak as functions of injection current density. Reproduced with permission [179]. Copyright 2019, Wiley-VCH.

at the InGaAs/SiN/Ag interface is strongly confined to the short axis and propagates along the long axis of the pillar. By using direct current electric injection with forward bias above ~10⁴ A cm⁻², super-linear emission with a line width of ~0.5 nm was observed from a device with the InGaAs pillar length of 6 µm and thickness of 310 nm at room temperature, as shown in Figure 6B. In addition, this work emphasized that the lasing threshold was negatively correlated with the thickness of InGaAs pillars owing to reduced mode confinement and increased ohmic losses. As a result, smaller devices lased only under a cryogenic environment because of insufficient heat dissipation at elevated temperatures, hindering practical applications. To overcome it and realize room-temperature CW lasing, Ding et al. further optimized the microfabrication process to minimize imperfections and fabricate devices close to the ideal situations by (1) using hydrogen silsesquioxane as photoresist in electron beam lithography to reduce the edge roughness of Cr/SiO₂ pattern within 2 nm; (2) improving the dry etching stage to restrict the tilting angle of the sidewall of InP/InGaAs/InP pillar to within 1° to suppress radiation loss; (3) increasing the SiN layer thickness from 20 to 30 nm to enhance the Q from 372 to 428; (4) increasing the grain size of the silver film to 1 µm, which is comparable with the feature size of plasmonic lasers to reduce the metal losses; and (5) performing thorough surface treatment such as oxygen plasma and dilute phosphoric acid processes to decrease surface recombination [171]. The authors have demonstrated significant transition from spontaneous emission to lasing at room temperature, and also clearly identified the achievement of lasing, which was fuzzy due to excessive peaks and weak super-linear lasing intensity in previous works [170]. Furthermore, they demonstrated a plasmonic laser ($V_{\rm eff}$: 0.146 $\lambda^{\rm 3}$) with azimuthally polarized beam based on cylindrical InP/InGaAs/InP pillar cladded by SiN/Ag (Figure 6C and inset, Figure 6D) [172]. They also tuned the lasing wavelength from 1.37 to 1.53 µm by varying the radius of the pillar, providing an approach for a multicolor metal-clad laser (Figure 6D). Despite the metal-cladded configuration, Yang et al. also reported one-dimensional, room-temperature, electrically driven plasmonic NW lasers of the MISW structure, as shown in Figure 6E [179]. The thicknesses of Ag, MgO, ZnO, MgO, and p-GaN layers were about 100, 7, 85, 5, and 2 nm, respectively. ZnO was chosen owing to its high optical gain coefficient and structural stability under high-energy injection. As shown in Figure 6F, electrons and holes were injected into the middle ZnO layer from Ag and p-GaN layers by

tunneling effect, respectively. The MgO layer blocked electrons in the active region to p-GaN to enhance the emission of the gain medium. As shown in Figure 6G, sharp peaks of transverse magnetic modes emerged with line width of ~1.12 nm above 70.2 A cm⁻², suggesting the achievement of lasing.

9 Applications

Plasmonic NW lasers have attracted great interest owing to their faster, more compact, and more power-efficient characteristics than conventional lasers as well as their demonstrated applications in chemical sensors and optical interconnects. In 2014, Ma et al. demonstrated a sub-part-per-billion chemical detector by using Ag-MgF₃-CdS nanolasers (Figure 7A) [202]. The output intensity of the plasmonic NW laser is strongly affected by surface recombination, in which the surface dangling bond or a S vacancy plays a key role in the large surfaceto-volume ratio of CdS NWs. In principle, the velocity of surface recombination is modified by the concentration of explosive molecules and electron deficiencies, leading to the variation of lasing intensity. As shown in Figure 7B, the variation ratio of the lasing intensity $\Delta I/I$ is generally linear with the vapor concentration of the analysts, e.g. equal to 1.2% ppb, 6.1% ppb, and 0.4% ppm for 2,4-dinitrotoluene, ammonium nitrate, and nitrobenzene, respectively. Plasmonic laser sensors exhibit good reversibility and stability during more than 5 h of experiments. In addition, Wang et al. proved plasmonic nanolasers as refractive index sensors in an aqueous condition using CdS and CdSe gain materials [205]. The lasing wavelength changes by 22 nm per refractive index unit at the response spectral regime (~718 nm). The figure of merit (FOM) of wavelength sensing is ~51, which is comparable to that of state-of-the-art SP resonance sensors (~50), and the FOM of intensity sensing is ~8000, which is nearly 40 times higher than that of SP resonance sensors.

Plasmonic NW lasers hold great promise for optical interconnects, but due to the large momentum mismatch at the interface, lasing photons are often diffracted in all directions, resulting in low coupling efficiency to the other optical units. To solve this problem, Kim et al. proposed a symmetry-broken, one-dimensional plasmonic laser consisting of SiO₂/Ag cladded InP/InGaAs/ InP pillar with $V_m \approx 0.28 \ (\lambda/n)^3$ and Q > 600, which was integrated onto bidirectional SOI waveguides supporting transverse electric mode at 204.8 THz (1.46 µm), as shown

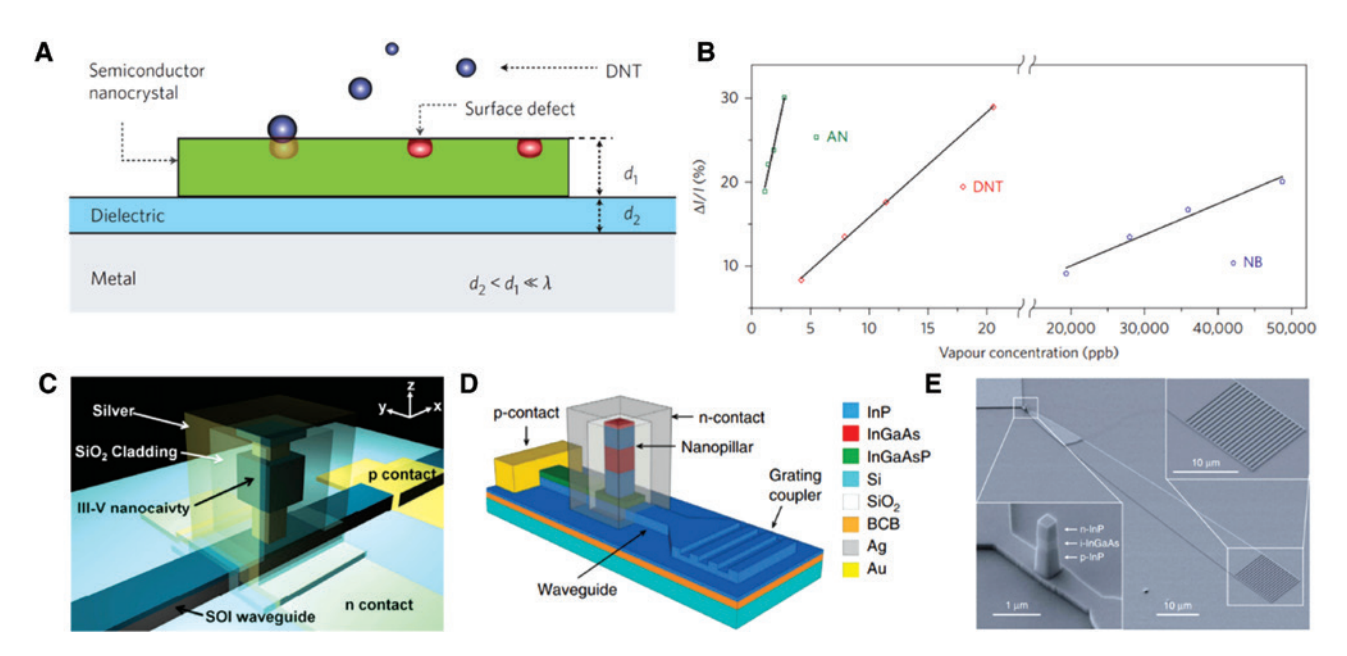


Figure 7: Applications of NW-like plasmonic waveguide.

(A) Schematic of an active explosives nanosensor based on the lasing intensity change from a plasmonic nanocavity, where the semiconductor nanocrystal acts as both the gain medium and the sensing material. (B) Calibration curves for the 2,4-dinitrotoluene, ammonium nitrate, and nitrobenzene detected by the nanosensor in air; the sensitivities are defined as the slope of these calibration curves. Reproduced with permission [202]. Copyright 2014, Springer Nature. (C) Schematic of a metal-cladded plasmonic laser coupled with Si waveguide. Reproduced with permission [203]. Copyright 2011, The Optical Society. (D) Schematic of a nanopillar LED based on an n-InP/InGaAs/p-InP nanopillar cladded by SiO₂/Ag on the silicon substrate. (E) Scanning electron microscope image of the nano-LED device before metallization. Insets: enlarged view of the nanopillar and the grating coupler. Reproduced with permission [204]. Copyright 2017, Springer Nature.

in Figure 7C [203]. Through breaking cavity symmetry by using asymmetry cladding or adopting pillars with rectangular cross-section, the wave vector of the plasmonic mode in the xy plane increased; hence the lasing photons preferred to radiate in the x-direction and couple into the SOI waveguide. Finally, the coupling efficiency of the plasmonic laser with SOI waveguide reached up to 78%. Indeed, replacing the bidirectional waveguide with a unidirectional waveguide could further enhance the theoretical coupling efficiency to ~90% [206]. Also, the as-reported coupling efficiency of the multiplexed waveguides embedded with plasmonic lasers is also higher than 70% (Figure 3C) [168]. Moreover, Dolores-Calzadilla et al. demonstrated a high-performance plasmonic nano-LED on silicon, which was constructed by SiO₂/Agcladded n-InP/i-InGaAs/p-InP pillars, as shown in Figure 7D, E [204]. Under a current injection of tens of µA, the on-chip external quantum efficiencies of the nano-LEDs were as high as 10⁻⁴ and 10⁻² at room temperature and 9.5 K, respectively. Meanwhile, direct modulation experiments revealed a switch-off time of 289 \pm 3 ps. Despite the failure of plasmonic lasing, the relatively high external quantum efficiency and the sub-nanosecond

electro-optical response are promising for low-power, high-speed optical interconnects.

10 Perspectives and challenges

In the past few years, a series of reports on plasmonic NW lasers have fully indicated their reliability and great promises as sub-diffraction-scale coherent light sources. In this review, we attempted to summarize the development of this newly rising field, including the fundamentals of semiconductor NW lasers and SPs, theoretical analysis and experimental demonstration of semiconductor NW plasmonic lasers, as well as latest frontiers to improve the performance of plasmonic lasers. Semiconductor material with a large gain coefficient and metal material with low ohmic losses at optical frequencies are expected for lowthreshold lasing. The geometry of NWs should be selected, and the closed-contact, smooth MIS interface can provide lower scattering loss and more efficient exciton-plasmon energy transfer to reduce the lasing threshold. Reducing NW's dimensionality may increase the lasing threshold because of weaker modal overlap, which brings challenges in controlling the size of NWs to demonstrate deep sub-wavelength lasers. However, rational selection of the cavity geometry, such as an ultrasmall pseudowedge waveguide, could enhance the spontaneous emission factor to realize low-threshold lasers in the deep sub-wavelength scale. Nevertheless, with the ultrasmall mode volume, strong localized electromagnetic field, high power density, and accelerated recombination rate, plasmonic lasers are suitable for a wide range of applications, i.e. nanolithography, high-resolution imaging, optical interconnection, and accurate metrologies [146, 207-209].

However, beyond these inspiring opportunities, there are also many immediate challenges for semiconductor NW plasmonic lasers. First, open questions still exist in the fabrication of high-quality crystals and heterojunctions for the plasmonic laser; for example, the integration of semiconductor NWs onto SOI substrates is limited by the inevitable lattice mismatch. Besides, surface and interface defects cannot be well controlled to modulate the functional properties of NWs to date, especially in plasmonic NW lasers with large-area metal-dielectric interfaces. Second, composition-graded NWs have been prepared to establish multicolor lasing, though the current fabrication technique is not simple enough. Other approaches by tuning the cavity design and utilizing the self-absorption effect only tailor the lasing wavelength over a narrow band, which is not enough for wideband multicolor lasers for practical applications. Third, although many strategies have been proposed to reduce the metal losses but showed great randomness, rational design and in-depth theoretical studies on low-threshold plasmonic lasing are still emerging. Last but not least, electrically driven plasmonic devices, especially with room-temperature CW operation, have a broader practical prospect in comparison to optically pumped lasers, while the cavity fabrication becomes much more complicated at the same time. In addition, in order to overcoming ohmic loss, a semiconductor core with stable structure and large gain coefficient under strong current injection is needed, and the embedded gap materials that prevent diffusion and conduct heat is also essential, but only a few types of semiconductor and dielectric materials meet these requirements according to current reports. Despite their inherent advantages and disadvantages, plasmonic NW lasers can be expected to become one of the central components for ultrasmall photoelectric devices and on-chip interconnections in the next decade.

Acknowledgments: This work was supported by the National Key Research and Development Program of China (2017YFA0304600, 2017YFA0205700), the National Natural Science Foundation of China (61774003, 61521004), the Open Research Fund Program of the State Key Laboratory of Low-dimensional Quantum Physics (No. KF201907) and the Opening project of State Key Laboratory of Bioelectronics of Southeast University.

References

- [1] Hall RN, Fenner GE, Kingsley JD, Soltys TJ, Carlson RO. Coherent light emission from gaas junctions. Phys Rev Lett 1962:9:366-8.
- [2] Soda H, Iga K-I, Kitahara C, Suematsu Y. GalnAsP/InP surface emitting injection lasers. Jpn J Appl Phys 1979;18:2329-30.
- [3] Koyama F, Kinoshita S, Iga K. Room-temperature continuous wave lasing characteristics of a GaAs vertical cavity surfaceemitting laser. Appl Phys Lett 1989;55:221-2.
- Huang MCY, Zhou Y, Chang-Hasnain CJ. A surface-emitting laser incorporating a high-index-contrast subwavelength grating. Nat Photonics 2007;1:119-22.
- [5] McCall SL, Levi AFJ, Slusher RE, Pearton SJ, Logan RA. Whispering-gallery mode microdisk lasers. Appl Phys Lett 1992;60:289-91.
- [6] Tamboli AC, Haberer ED, Sharma R, Lee KH, Nakamura S, Hu EL. Room-temperature continuous-wave lasing in GaN/InGaN microdisks. Nat Photonics 2007;1:61-4.
- [7] Van Campenhout J, Rojo-Romeo P, Regreny P, et al. Electrically pumped InP-based microdisk lasers integrated with a nanophotonic silicon-on-insulator waveguide circuit. Opt Express 2007;15:6744-9.
- [8] Painter O, Lee RK, Scherer A, et al. Two-dimensional photonic band-Gap defect mode laser. Science 1999;284:1819-21.
- [9] Park H-G, Kim S-H, Kwon S-H, et al. Electrically driven singlecell photonic crystal laser. Science 2004;305:1444-7.
- [10] Altug H, Englund D, Vučković J. Ultrafast photonic crystal nanocavity laser. Nat Phys 2006;2:484-8.
- [11] Johnson JC, Choi H-J, Knutsen KP, Schaller RD, Yang P, Saykally RJ. Single gallium nitride nanowire lasers. Nat Mater 2002;1:106-10.
- [12] Saxena D, Mokkapati S, Parkinson P, et al. Optically pumped room-temperature GaAs nanowire lasers. Nat Photonics 2013;7:963-8.
- [13] Li KH, Liu X, Wang Q, Zhao S, Mi Z. Ultralow-threshold electrically injected AlGaN nanowire ultraviolet lasers on Si operating at low temperature. Nat Nanotechnol 2015;10:140-4.
- [14] Ning C-Z. Semiconductor nanolasers and the size-energy-efficiency challenge: a review. Adv Photonics 2019;1:014002.
- [15] Berini P, De Leon I. Surface plasmon-polariton amplifiers and lasers. Nat Photonics 2011;6:16-24.
- [16] Oulton RF. Surface plasmon lasers: sources of nanoscopic light. Mater Today 2012;15:26-34.
- [17] Ma R-M, Oulton RF, Sorger VJ, Zhang X. Plasmon lasers: coherent light source at molecular scales. Laser Photonics Rev 2013;7:1-21.
- [18] Gwo S, Shih C-K. Semiconductor plasmonic nanolasers: current status and perspectives. Rep Prog Phys 2016;79:086501.
- Ritchie RH. Plasma losses by fast electrons in thin films. Phys Rev 1957;106:874-81.

- [20] Barnes WL. Surface plasmon-polariton length scales: a route to sub-wavelength optics. J Opt A: Pure Appl Opt 2006;8: S87-93.
- [21] Bergman DJ, Stockman MI. Surface plasmon amplification by stimulated emission of radiation: quantum generation of coherent surface plasmons in nanosystems. Phys Rev Lett 2003;90:027402.
- [22] Barnes WL, Dereux A, Ebbesen TW. Surface plasmon subwavelength optics. Nature 2003:424:824-30.
- [23] Zayats AV, Smolyaninov II, Maradudin AA. Nano-optics of surface plasmon polaritons. Phys Rep 2005;408:131-314.
- [24] Gramotnev DK, Bozhevolnyi SI. Plasmonics beyond the diffraction limit. Nat Photonics 2010;4:83-91.
- [25] Stockman MI. Nanoplasmonics: past, present, and glimpse into future. Opt Express 2011:19:22029-106.
- [26] Kauranen M, Zavats AV. Nonlinear plasmonics. Nat Photonics 2012:6:737-48.
- [27] Shang Q, Zhang S, Liu Z, et al. Surface plasmon enhanced strong exciton-photon coupling in hybrid inorganic-organic perovskite nanowires. Nano Lett 2018;18:3335-43.
- [28] Noginov MA, Zhu G, Belgrave AM, et al. Demonstration of a spaser-based nanolaser. Nature 2009;460:1110-2.
- [29] Galanzha EI, Weingold R, Nedosekin DA, et al. Spaser as a biological probe. Nat Commun 2017;8:15528.
- [30] Meng X, Kildishev AV, Fujita K, Tanaka K, Shalaev VM. Wavelength-tunable spasing in the visible. Nano Lett 2013;13:
- [31] Oulton RF, Sorger VJ, Zentgraf T, et al. Plasmon lasers at deep subwavelength scale. Nature 2009;461:629-32.
- [32] Hill MT, Marell M, Leong ESP, et al. Lasing in metal-insulatormetal sub-wavelength plasmonic waveguides. Opt Express 2009;17:11107-12.
- [33] Zhou W, Dridi M, Suh JY, et al. Lasing action in strongly coupled plasmonic nanocavity arrays. Nat Nanotechnol 2013;8:506-11.
- [34] van Beijnum F, van Veldhoven PJ, Geluk EJ, de Dood MJA, Hooft GW, van Exter MP. Surface plasmon lasing observed in metal hole arrays. Phys Rev Lett 2013;110:206802.
- [35] Yang A, Hoang TB, Dridi M, et al. Real-time tunable lasing from plasmonic nanocavity arrays. Nat Commun 2015;6:6939.
- [36] Hakala TK, Rekola HT, Väkeväinen AI, et al. Lasing in dark and bright modes of a finite-sized plasmonic lattice. Nat Commun 2017;8:13687.
- [37] Yan R, Gargas D, Yang P. Nanowire photonics. Nat Photonics 2009;3:569-76.
- [38] Lieber CM, Wang ZL. Functional nanowires. MRS Bull 2011;32:99-108.
- [39] Xia Y, Yang P, Sun Y, et al. One-Dimensional nanostructures: synthesis, characterization, and applications. Adv Mater 2003;15:353-89.
- [40] Dasgupta NP, Sun J, Liu C, et al. 25th anniversary article: semiconductor nanowires-synthesis, characterization, and applications. Adv Mater 2014;26:2137-84.
- [41] Tonucci RJ, Justus BL, Campillo AJ, Ford CE. Ngnochannel array glass. Science 1992;258:783-5.
- [42] Morton KJ, Nieberg G, Bai S, Chou SY. Wafer-scale patterning of sub-40 nm diameter and high aspect ratio (>50:1) silicon pillar arrays by nanoimprint and etching. Nanotechnology 2008;19:345301.
- [43] Winston D, Manfrinato VR, Nicaise SM, et al. Neon Ion Beam Lithography (NIBL). Nano Lett 2011;11:4343-7.

- [44] Scappucci G, Capellini G, Johnston B, Klesse WM, Miwa JA, Simmons MY. A complete fabrication route for atomic-scale, donor-based devices in single-crystal germanium. Nano Lett 2011:11:2272-9.
- [45] Sun Y, Graff RA, Strano MS, Rogers JA. Top-down fabrication of semiconductor nanowires with alternating structures along their longitudinal and transverse axes. Small 2005;1:1052-7.
- [46] Naureen S, Sanatinia R, Shahid N, Anand S. High optical quality InP-based nanopillars fabricated by a top-down approach. Nano Lett 2011;11:4805-11.
- [47] Damilano B, Vézian S, Brault J, Alloing B, Massies J. Selective area sublimation: a simple top-down route for GaN-based nanowire fabrication. Nano Lett 2016;16:1863-68.
- [48] Zhang M-L, Peng K-Q, Fan X, et al. Preparation of large-area uniform silicon nanowires arrays through metal-assisted chemical etching. J Phys Chem C 2008;112:4444-50.
- [49] Yan H, He R, Johnson J, Law M, Saykally RJ, Yang P. Dendritic nanowire ultraviolet laser array. J Am Chem Soc 2003;125:4728-9.
- [50] Liu Z, Shang Q, Li C, et al. Temperature-dependent photoluminescence and lasing properties of CsPbBr, nanowires. Appl Phys Lett 2019;114:101902.
- [51] Pan ZW, Dai ZR, Wang ZL. Nanobelts of semiconducting oxides. Science 2001;291:1947-9.
- [52] Heath JR, LeGoues FK. A liquid solution synthesis of single crystal germanium quantum wires. Chem Phys Lett 1993;208:263-8.
- [53] Tang Z, Kotov NA, Giersig M. Spontaneous organization of single CdTe nanoparticles into luminescent nanowires. Science 2002;297:237-40.
- [54] Trentler TJ, Hickman KM, Goel SC, Viano AM, Gibbons PC, Buhro WE. Solution-liquid-solid growth of crystalline III-V semiconductors: an analogy to vapor-liquid-solid growth. Science 1995;270:1791-4.
- [55] Pan J, Utama MIB, Zhang Q, et al. Composition-tunable vertically aligned CdSxSe1-x nanowire arrays via van der waals epitaxy: investigation of optical properties and photocatalytic behavior. Adv Mater 2012;24:4151-6.
- [56] Burgess T, Saxena D, Mokkapati S, et al. Doping-enhanced radiative efficiency enables lasing in unpassivated GaAs nanowires. Nat Commun 2016;7:11927.
- [57] Tsivion D, Schvartzman M, Popovitz-Biro R, von Huth P, Joselevich E. Guided growth of millimeter-long horizontal nanowires with controlled orientations. Science 2011;333:1003-7.
- [58] Morales AM, Lieber CM. A laser ablation method for the synthesis of crystalline semiconductor nanowires. Science 1998:279:208-11.
- [59] Gao Y, Zhao L, Shang Q, et al. Ultrathin CsPbX3 nanowire arrays with strong emission anisotropy. Adv Mater 2018;30:1801805.
- [60] Qian F, Li Y, Gradečak S, et al. Multi-quantum-well nanowire heterostructures for wavelength-controlled lasers. Nat Mater 2008;7:701-6.
- [61] Kayes BM, Atwater HA, Lewis NS. Comparison of the device physics principles of planar and radial p-n junction nanorod solar cells. J Appl Phys 2005;97:114302.
- [62] Perea DE, Hemesath ER, Schwalbach EJ, Lensch-Falk JL, Voorhees PW, Lauhon LJ. Direct measurement of dopant distribution in an individual vapour-liquid-solid nanowire. Nat Nanotechnol 2009;4:315-9.

- [63] Mariani G, Scofield AC, Hung C-H, Huffaker DL. GaAs nanopillararray solar cells employing in situ surface passivation. Nat Commun 2013:4:1497.
- [64] Shinada T, Okamoto S, Kobayashi T, Ohdomari I. Enhancing semiconductor device performance using ordered dopant arrays. Nature 2005;437:1128-31.
- [65] He J, Lilley CM. Surface effect on the elastic behavior of static bending nanowires. Nano Lett 2008;8:1798-802.
- [66] Hong W-K, Sohn JI, Hwang D-K, et al. Tunable electronic transport characteristics of surface-architecture-controlled ZnO nanowire field effect transistors. Nano Lett 2008;8:950-6.
- [67] Bu L, Guo S, Zhang X, et al. Surface engineering of hierarchical platinum-cobalt nanowires for efficient electrocatalysis. Nat Commun 2016;7:11850.
- [68] Zhang A, Zheng G, Lieber CM. Nanoelectronics, circuits and nanoprocessors. In: Zhang A, Zheng G, Lieber CM. Nanowires: building blocks for nanoscience and nanotechnology. Cham: Springer International Publishing, 2016:103-42.
- [69] Pauzauskie PJ, Yang P. Nanowire photonics. Mater Today 2006;9:36-45.
- [70] Eaton SW, Fu A, Wong AB, Ning C-Z, Yang P. Semiconductor nanowire lasers. Nat Rev Mater 2016;1:16028.
- [71] Couteau C, Larrue A, Wilhelm C, Soci C. Nanowire lasers. Nanophotonics 2015;4:90-107.
- [72] Fu Y, Zhu H, Stoumpos CC, et al. Broad wavelength tunable robust lasing from single-crystal nanowires of cesium lead halide perovskites (CsPbX3, X=Cl, Br, I). ACS Nano 2016;10: 7963-72.
- [73] Liu X, Zhang Q, Xiong Q, Sum TC. Tailoring the lasing modes in semiconductor nanowire cavities using intrinsic self-absorption. Nano Lett 2013;13:1080-5.
- [74] Liu X, Zhang Q, Yip JN, Xiong Q, Sum TC. Wavelength Tunable single nanowire lasers based on surface plasmon polariton enhanced burstein-moss effect. Nano Lett 2013;13:5336-43.
- [75] Huang MH, Mao S, Feick H, et al. Room-temperature ultraviolet nanowire nanolasers. Science 2001;292:1897-9.
- [76] Chu S, Wang G, Zhou W, et al. Electrically pumped waveguide lasing from ZnO nanowires. Nat Nanotechnol 2011;6:506-10.
- [77] Zong H, Yang Y, Ma C, et al. Flexibly and repeatedly modulating lasing wavelengths in a single core-shell semiconductor microrod. ACS Nano 2017;11:5808-14.
- [78] Luan CY, Liu YK, Jiang Y, et al. Composition tuning of roomtemperature nanolasers. Vacuum 2012;86:737-41.
- [79] Zapien JA, Liu YK, Shan YY, Tang H, Lee CS, Lee ST. Continuous near-infrared-to-ultraviolet lasing from II-VI nanoribbons. Appl Phys Lett 2007;90:213114.
- [80] Agarwal R, Barrelet CJ, Lieber CM. Lasing in single cadmium sulfide nanowire optical cavities. Nano Lett 2005;5:917-20.
- [81] Liu Z, Yin L, Ning H, Yang Z, Tong L, Ning C-Z. Dynamical colorcontrollable lasing with extremely wide tuning range from red to green in a single alloy nanowire using nanoscale manipulation. Nano Lett 2013;13:4945-50.
- [82] Gu F, Yang Z, Yu H, et al. Spatial bandgap engineering along single alloy nanowires. J Am Chem Soc 2011;133:2037-9.
- [83] Yang Z, Wang D, Meng C, et al. Broadly defining lasing wavelengths in single bandgap-graded semiconductor nanowires. Nano Lett 2014;14:3153-9.
- [84] Xu J, Ma L, Guo P, et al. Room-temperature dual-wavelength lasing from single-nanoribbon lateral heterostructures. J Am Chem Soc 2012;134:12394-7.

- [85] Xiao Y, Meng C, Wang P, et al. Single-nanowire single-mode laser. Nano Lett 2011;11:1122-6.
- [86] Chen R, Bakti Utama MI, Peng Z, Peng B, Xiong Q, Sun H. Excitonic properties and near-infrared coherent random lasing in vertically aligned CdSe nanowires. Adv Mater 2011;23: 1404-08.
- [87] Zhao YS, Peng A, Fu H, Ma Y, Yao J. Nanowire waveguides and ultraviolet lasers based on small organic molecules. Adv Mater 2008:20:1661-5.
- [88] Quochi F, Cordella F, Mura A, Bongiovanni G, Balzer F, Rubahn HG. Gain amplification and lasing properties of individual organic nanofibers. Appl Phys Lett 2006;88:041106.
- [89] Zhang C, Zou C-L, Yan Y, et al. Two-photon pumped lasing in single-crystal organic nanowire exciton polariton resonators. I Am Chem Soc 2011:133:7276-9.
- [90] Zhang W, Yan Y, Gu J, Yao J, Zhao YS. Low-threshold wavelength-switchable organic nanowire lasers based on excitedstate intramolecular proton transfer. Angew Chem Int Ed Engl 2015;54:7125-9.
- [91] Kanazawa S, Ichikawa M, Koyama T, Taniguchi Y. Self-waveguided photoemission and lasing of organic crystalline wires obtained by an improved expitaxial growth method. ChemPhysChem 2006;7:1881-4.
- [92] Huang R, Wang C, Wang Y, Zhang H. Elastic self-doping organic single crystals exhibiting flexible optical waveguide and amplified spontaneous emission. Adv Mater 2018;30:e1800814.
- [93] Wang X, Liao Q, Lu X, Li H, Xu Z, Fu H. Shape-engineering of self-assembled organic single microcrystal as optical microresonator for laser applications. Sci Rep 2014;4:7011.
- [94] Wang X, Li Z-Z, Zhuo M-P, et al. Tunable near-infrared organic nanowire nanolasers. Adv Funct Mater 2017;27:1703470.
- [95] Zhu H, Fu Y, Meng F, et al. Lead halide perovskite nanowire lasers with low lasing thresholds and high quality factors. Nat Mater 2015;14:636-2.
- [96] Fu Y, Zhu H, Schrader AW, et al. Nanowire lasers of formamidinium lead halide perovskites and their stabilized alloys with improved stability. Nano Lett 2016;16:1000-8.
- [97] Xing J, Liu XF, Zhang Q, et al. Vapor phase synthesis of organometal halide perovskite nanowires for tunable roomtemperature nanolasers. Nano Lett 2015;15:4571-7.
- [98] Liu P, He X, Ren J, Liao Q, Yao J, Fu H. Organic-inorganic hybrid perovskite nanowire laser arrays. ACS Nano 2017;11:5766-73.
- [99] Fan F, Turkdogan S, Liu Z, Shelhammer D, Ning CZ. A monolithic white laser. Nat Nanotechnol 2015;10:796-803.
- [100] Mahan GD. Phonon-broadened optical spectra: urbach's rule. Phys Rev 1966;145:602-8.
- [101] Dunn D. Urbach's rule in an electron-phonon model. Phys Rev 1968;174:855-8.
- [102] John S, Chou MY, Cohen MH, Soukoulis CM. Density of states for an electron in a correlated Gaussian random potential: theory of the urbach tail. Phys Rev B 1988;37:6963-76.
- [103] Urbach F. The long-wavelength edge of photographic sensitivity and of the electronic absorption of solids. Phys Rev 1953;92:1324.
- [104] Li J, Meng C, Liu Y, et al. Wavelength tunable CdSe nanowire lasers based on the absorption-emission-absorption process. Adv Mater 2013;25:833-7.
- [105] Burstein E. Anomalous optical absorption limit in InSb. Phys Rev 1954;93:632-3.

- [106] Moss TS. The interpretation of the properties of indium antimonide. Proc Phys Soc Section B 1954;67:775-82.
- [107] Sun QC, Yadgarov L, Rosentsveig R, Seifert G, Tenne R, Musfeldt JL. Observation of a Burstein-Moss shift in Rhenium-Doped MoS2 nanoparticles. ACS Nano 2013;7:3506-11.
- [108] Yang YH, Chen XY, Feng Y, Yang GW. Physical mechanism of blue-shift of UV luminescence of a single pencil-like ZnO nanowire. Nano Lett 2007;7:3879-83.
- [109] Manser JS, Kamat PV. Band filling with free charge carriers in organometal halide perovskites. Nat Photonics 2014;8:737-43.
- [110] Feneberg M, Osterburg S, Lange K, et al. Band gap renormalization and Burstein-Moss effect in silicon- and germanium-doped wurtzite GaN up to1020 cm - 3. Phys Rev B 2014;90:075203.
- [111] Kuykendall T, Pauzauskie PJ, Zhang Y, et al. Crystallographic alignment of high-density gallium nitride nanowire arrays. Nat Mater 2004;3:524-8.
- [112] Lorenz M, Kaidashev EM, Rahm A, et al. MgxZn1 – $xO(0 \le x < 0.2)$ nanowire arrays on sapphire grown by high-pressure pulsed-laser deposition. Appl Phys Lett 2005;86:143113.
- [113] Frost T, Jahangir S, Stark E, et al. Monolithic electrically injected nanowire array edge-emitting laser on (001) silicon. Nano Lett 2014;14:4535-41.
- [114] Routkevitch D, Bigioni T, Moskovits M, Xu JM. Electrochemical fabrication of CdS nanowire arrays in porous anodic aluminum oxide templates. J Phys Chem 1996;100:14037-47.
- [115] Greene LE, Law M, Tan DH, et al. General route to vertical ZnO nanowire arrays using textured ZnO seeds. Nano Lett 2005;5:1231-6.
- [116] Wang X, Summers CJ, Wang ZL. Large-scale hexagonalpatterned growth of aligned ZnO nanorods for nanooptoelectronics and nanosensor arrays. Nano Lett 2004; 4:423-6.
- [117] Kuo T-J, Lin C-N, Kuo C-L, Huang MH. Growth of ultralong ZnO nanowires on silicon substrates by vapor transport and their use as recyclable photocatalysts. Chem Mater 2007;19:5143-7.
- [118] Huang Z, Zhang X, Reiche M, et al. Extended arrays of vertically aligned sub-10 nm diameter [100] Si nanowires by metalassisted chemical etching. Nano Lett 2008;8:3046-51.
- [119] Wang J. Plissard SR, Verheijen MA, Feiner L-F, Cavalli A, Bakkers EPAM. Reversible switching of InP nanowire growth direction by catalyst engineering. Nano Lett 2013;13:3802-6.
- [120] Kim H, Lee W-J, Farrell AC, et al. Monolithic InGaAs nanowire array lasers on silicon-on-insulator operating at room temperature. Nano Lett 2017;17:3465-70.
- [121] Ryan KM, Mastroianni A, Stancil KA, Liu H, Alivisatos AP. Electric-field-assisted assembly of perpendicularly oriented nanorod superlattices. Nano Lett 2006;6:1479-82.
- [122] Huang Y, Duan X, Wei Q, Lieber CM. Directed assembly of onedimensional nanostructures into functional networks. Science 2001;291:630-3.
- [123] Fan Z, Ho JC, Jacobson ZA, et al. Wafer-scale assembly of highly ordered semiconductor nanowire arrays by contact printing. Nano Lett 2008;8:20-5.
- [124] Yu G, Cao A, Lieber CM. Large-area blown bubble films of aligned nanowires and carbon nanotubes. Nat Nanotechnol 2007;2:372-7.
- [125] Panda AB, Acharya S, Efrima S, Golan Y. Synthesis, assembly, and optical properties of shape- and phase-controlled ZnSe nanostructures. Langmuir 2007;23:765-70.

- [126] York SM, Leibsle FM. Co nanowire arrays on N-terminated Cu(110) surfaces. Phys Rev B 2001;64:033411.
- [127] Fortuna SA, Wen J, Chun IS, Li X. Planar GaAs nanowires on GaAs (100) substrates: self-aligned, nearly twin-defect free, and transfer-printable. Nano Lett 2008;8:4421-7.
- [128] Zhang C, Miao X, Mohseni PK, Choi W, Li X. Site-controlled VLS growth of planar nanowires: yield and mechanism. Nano Lett 2014;14:6836-41.
- [129] Zhu G, Yang R, Wang S, Wang ZL. Flexible high-output nanogenerator based on lateral ZnO nanowire array. Nano Lett 2010;10:3151-5.
- [130] Min KW, Kim YK, Shin G, et al. White-light emitting diode array of P+-Si/aligned N-SnO 2 nanowires heterojunctions. Adv Funct Mater 2011;21:119-24.
- [131] Guilhabert B, Hurtado A, Jevtics D, et al. Transfer printing of semiconductor nanowires with lasing emission for controllable nanophotonic device fabrication. ACS Nano 2016;10:3951-8.
- [132] Willets KA, Van Duyne RP. Localized surface plasmon resonance spectroscopy and sensing. Annu Rev Phys Chem 2007;58:267-97.
- [133] Raether H, editor. Surface plasmons on smooth and rough surfaces and on gratings. Berlin, Heidelberg: Springer Berlin Heidelberg, 1988:4-39.
- [134] Murphy CJ, Sau TK, Gole AM, et al. Anisotropic metal nanoparticles: synthesis, assembly, and optical applications. J Phys Chem B 2005;109:13857-70.
- [135] Moskovits M. Surface-enhanced spectroscopy. Rev Mod Phys 1985;57:783-826.
- [136] Nie S, Emory SR. Probing single molecules and single nanoparticles by surface-enhanced raman scattering. Science 1997;275:1102-6.
- [137] Kneipp K, Wang Y, Kneipp H, et al. Single molecule detection using surface-enhanced raman scattering (SERS). Phys Rev Lett 1997;78:1667-70.
- [138] Xu H, Bjerneld EJ, Käll M, Börjesson L. Spectroscopy of single hemoglobin molecules by surface enhanced raman scattering. Phys Rev Lett 1999;83:4357-60.
- [139] Lal S, Link S, Halas NJ. Nano-optics from sensing to waveguiding. Nat Photon 2007;1:641-8.
- [140] Jain PK, Huang X, El-Sayed IH, El-Sayed MA. Noble metals on the nanoscale: optical and photothermal properties and some applications in imaging, sensing, biology, and medicine. Acc Chem Res 2008;41:1578-86.
- [141] Jiang R, Li B, Fang C, Wang J. Metal/semiconductor hybrid nanostructures for plasmon-enhanced applications. Adv Mater 2014:26:5274-309.
- [142] Larsson EM, Langhammer C, Zorić I, Kasemo B. Nanoplasmonic probes of catalytic reactions. Science 2009;326:1091-4.
- [143] Sönnichsen C, Reinhard BM, Liphardt J, Alivisatos AP. A molecular ruler based on plasmon coupling of single gold and silver nanoparticles. Nat Biotechnol 2005;23:741-5.
- [144] Wei H, Li Z, Tian X, et al. Quantum dot-based local field imaging reveals plasmon-based interferometric logic in silver nanowire networks. Nano Lett 2011;11:471-5.
- [145] Naik GV, Shalaev VM, Boltasseva A. Alternative plasmonic materials: beyond gold and silver. Adv Mater 2013;25: 3264-94.
- [146] Polman A. Applied physics. Plasmonics applied. Science 2008;322:868-9.

- [147] Boltasseva A, Atwater HA. Materials science. Low-loss plasmonic metamaterials. Science 2011;331:290-1.
- [148] Pitarke JM, Silkin VM, Chulkov EV, Echenique PM. Theory of surface plasmons and surface-plasmon polaritons. Rep Prog Phys 2006;70:1-87.
- [149] Berini P. Long-range surface plasmon polaritons. Adv Opt Photonics 2009;1:484-588.
- [150] Maier SA, editor. Plasmonics: fundamentals and applications. New York, NY, USA: Springer, 2007:21-37.
- [151] Oulton RF, Sorger VJ, Genov DA, Pile DFP, Zhang X. Optimization of a Si-SiO2 waveguide coupler for photonic integrated circuits. Nat Photon 2008;2:496-500.
- [152] Sorger VJ, Ye Z, Oulton RF, et al. Experimental demonstration of low-loss optical waveguiding at deep sub-wavelength scales. Nat Commun 2011:2:331.
- [153] Chen HZ, Hu JQ, Wang S. Imaging the dark emission of spasers. Sci Adv 2017;3:e1601962.
- [154] Lu Y-J, Kim J, Chen H-Y, et al. Plasmonic nanolaser using epitaxially grown silver film. Science 2012;337:450-3.
- [155] Zhang Q, Li G, Liu X, et al. A room temperature low-threshold ultraviolet plasmonic nanolaser. Nat Commun 2014;5:4953.
- [156] Ho J, Tatebayashi J, Sergent S, Fong CF, Iwamoto S, Arakawa Y. Low-threshold near-infrared GaAs-AlGaAs core-shell nanowire plasmon laser. ACS Photonics 2015;2:165-71.
- [157] Chou Y-H, Wu Y-M, Hong K-B, et al. High-operation-temperature plasmonic nanolasers on single-crystalline aluminum. Nano Lett 2016;16:3179-86.
- [158] Lu J, Jiang M, Wei M, et al. Plasmon-induced accelerated exciton recombination dynamics in ZnO/Ag hybrid nanolasers. ACS Photonics 2017;4:2419-24.
- [159] Yu H, Sidiropoulos TPH, Liu W, et al. Influence of silver film quality on the threshold of plasmonic nanowire lasers. Adv Opt Mater 2017;5:1600856.
- [160] Zhang Q, Shang Q, Shi J, et al. Wavelength tunable plasmonic lasers based on intrinsic self-absorption of gain material. ACS Photonics 2017;4:2789-96.
- [161] Wu Z, Chen J, Mi Y, et al. All-inorganic CsPbBr, nanowire based plasmonic lasers. Adv Opt Mater 2018;6:1800674.
- [162] Neumann A, Wierer JJ, Davis W, Ohno Y, Brueck SRJ, Tsao JY. Four-color laser white illuminant demonstrating high colorrendering quality. Opt Express 2011;19:A982-90.
- [163] Dang C, Lee J, Breen C, Steckel JS, Coe-Sullivan S, Nurmikko A. Red, green and blue lasing enabled by single-exciton gain in colloidal quantum dot films. Nat Nanotechnol 2012;7: 335-9.
- [164] Zhang C, Zou CL, Zhao Y, et al. Organic printed photonics: from microring lasers to integrated circuits. Sci Adv 2015;1:e1500257.
- [165] Yang Z, Xu J, Wang P, Zhuang X, Pan A, Tong L. On-nanowire spatial band gap design for white light emission. Nano Lett 2011;11:5085-9.
- [166] Sirbuly DJ, Law M, Pauzauskie P, et al. Optical routing and sensing with nanowire assemblies. Proceedings of the National Academy of Sciences 2005;102:7800-5.
- [167] Lu YJ, Wang CY, Kim J, et al. All-color plasmonic nanolasers with ultralow thresholds: autotuning mechanism for singlemode lasing. Nano Lett 2014;14:4381-8.
- [168] Ma R-M, Yin X, Oulton RF, Sorger VJ, Zhang X. Multiplexed and electrically modulated plasmon laser circuit. Nano Lett 2012;12:5396-402.

- [169] Wu CY, Kuo CT, Wang CY, et al. Plasmonic green nanolaser based on a metal-oxide-semiconductor structure. Nano Lett 2011:11:4256-60.
- [170] Ding K, Liu ZC, Yin LJ, et al. Room-temperature continuous wave lasing in deep-subwavelength metallic cavities under electrical injection. Phys Rev B 2012;85:041301.
- [171] Ding K, Hill MT, Liu ZC, Yin LJ, van Veldhoven PJ, Ning CZ. Record performance of electrical injection sub-wavelength metallic-cavity semiconductor lasers at room temperature. Opt Express 2013;21:4728-33.
- [172] Ding K, Yin L, Hill MT, Liu Z, van Veldhoven PJ, Ning CZ. An electrical injection metallic cavity nanolaser with azimuthal polarization. Appl Phys Lett 2013;102:041110.
- [173] Wu X, Xiao Y, Meng C, et al. Hybrid photon-plasmon nanowire lasers. Nano Lett 2013:13:5654-9.
- [174] Yu H, Ren K, Wu Q, et al. Organic-inorganic perovskite plasmonic nanowire lasers with a low threshold and a good thermal stability. Nanoscale 2016;8:19536-40.
- [175] Kress SJP, Cui J, Rohner P, et al. A customizable class of colloidal-quantum-dot spasers and plasmonic amplifiers. Sci Adv 2017;3:e1700688.
- [176] Lee CJ, Yeh H, Cheng F, et al. Low-threshold plasmonic lasers on a single-crystalline epitaxial silver platform at telecom wavelength. ACS Photonics 2017;4:1431-9.
- [177] Huang C, Sun W, Fan Y, et al. Formation of lead halide perovskite based plasmonic nanolasers and nanolaser arrays by tailoring the substrate. ACS Nano 2018;12: 3865-74.
- [178] Liu S, Sheng B, Wang X, et al. Molecular beam epitaxy of single-crystalline aluminum film for low threshold ultraviolet plasmonic nanolasers. Appl Phys Lett 2018;112:231904.
- [179] Yang X, Ni PN, Jing PT, et al. Room temperature electrically driven ultraviolet plasmonic lasers. Adv Opt Mater 2019;0:1801681.
- [180] Khurgin JB. How to deal with the loss in plasmonics and metamaterials. Nat. Nanotechnol 2015;10:2-6.
- [181] Johnson PB, Christy RW. Optical constants of the noble metals. Phys Rev B 1972;6:4370-9.
- [182] Robinson JT, Preston K, Painter O, Lipson M. First-principle derivation of gain in high-index-contrast waveguides. Opt Express 2008;16:16659-69.
- [183] Govorov AO, Lee J, Kotov NA. Theory of plasmon-enhanced Förster energy transfer in optically excited semiconductor and metal nanoparticles. Phys Rev B 2007;76:125308.
- [184] Chou B-T, Chou Y-H, Wu Y-M, et al. Single-crystalline aluminum film for ultraviolet plasmonic nanolasers. Sci Rep 2016:6:19887.
- [185] Wang S, Wang X-Y, Li B, et al. Unusual scaling laws for plasmonic nanolasers beyond the diffraction limit. Nat Commun
- [186] Chou Y-H, Hong K-B, Chang C-T, et al. Ultracompact pseudowedge plasmonic lasers and laser arrays. Nano Lett 2018;18:747-53.
- [187] Sasikala V, Chitra K. All optical switching and associated technologies: a review. J Opt 2018;47:307-17.
- [188] Khurgin JB, Sun G. Comparative analysis of spasers, verticalcavity surface-emitting lasers and surface-plasmon-emitting diodes. Nat Photonics 2014;8:468-73.
- [189] Purcell EM. Spontaneous emission probabilities at radio frequencies. Phys Rev 1946;69:681.

- [190] Sidiropoulos TPH, Röder R, Geburt S, et al. Ultrafast plasmonic nanowire lasers near the surface plasmon frequency. Nat Phys 2014;10:870-6.
- [191] Liu K, Li N, Sadana DK, Sorger VJ. Integrated nanocavity plasmon light sources for on-chip optical interconnects. ACS Photonics 2016;3:233-42.
- [192] Vesseur EJR, de Abajo FJG, Polman A. Broadband Purcell enhancement in plasmonic ring cavities. Phys Rev B 2010:82:165419.
- [193] Akselrod GM, Argyropoulos C, Hoang TB, et al. Probing the mechanisms of large Purcell enhancement in plasmonic nanoantennas. Nat Photonics 2014;8:835-40.
- [194] Vahala KJ. Optical microcavities. Nature 2003;424:
- [195] Böckler C, Reitzenstein S, Kistner C, et al. Electrically driven high-Q quantum dot-micropillar cavities. Appl Phys Lett 2008;92:091107.
- [196] Ma R-M, Oulton RF, Sorger VJ, Bartal G, Zhang X. Roomtemperature sub-diffraction-limited plasmon laser by total internal reflection. Nat Mater 2010;10:110-3.
- [197] Chou Y-H, Chou B-T, Chiang C-K, et al. Ultrastrong mode confinement in ZnO surface plasmon nanolasers. ACS Nano 2015;9:3978-83.
- [198] Genov DA, Oulton RF, Bartal G, Zhang X. Anomalous spectral scaling of light emission rates in low-dimensional metallic nanostructures. Phys Rev B 2011;83:245312.

- [199] Hill MT, Gather MC. Advances in small lasers. Nat Photonics 2014;8:908-18.
- [200] Zhang Y, Saxena D, Aagesen M, Liu H. Toward electrically driven semiconductor nanowire lasers. Nanotechnology 2019;30:192002.
- [201] Hill MT, Oei Y-S, Smalbrugge B, et al. Lasing in metallic-coated nanocavities. Nat Photonics 2007;1:589-94.
- [202] Ma RM, Ota S, Li Y, Yang S, Zhang X. Explosives detection in a lasing plasmon nanocavity. Nat Nanotechnol 2014;9:600-4.
- [203] Kim M-K, Lakhani AM, Wu MC. Efficient waveguide-coupling of metal-clad nanolaser cavities. Opt Express 2011;19:23504-12.
- [204] Dolores-Calzadilla V, Romeira B, Pagliano F, et al. Waveguidecoupled nanopillar metal-cavity light-emitting diodes on silicon. Nat Commun 2017;8:14323.
- [205] Wang S, Li B, Wang X-Y, et al. High-yield plasmonic nanolasers with superior stability for sensing in aqueous solution. ACS Photonics 2017;4:1355-60.
- [206] Kim M-K, Li Z, Huang K, Going R, Wu MC, Choo H. Engineering of metal-clad optical nanocavity to optimize coupling with integrated waveguides. Opt Express 2013;21:25796-804.
- [207] Tame MS, McEnery KR, Özdemir ŞK, Lee J, Maier SA, Kim MS. Quantum plasmonics. Nat Phys 2013;9:329-40.
- [208] Grigorenko AN, Polini M, Novoselov KS. Graphene plasmonics. Nat Photonics 2012;6:749-58.
- [209] Ozbay E. Plasmonics: merging photonics and electronics at nanoscale dimensions. Science 2006;311:189-93.